Interface and Surface Properties of Short Polymers in Solution: Monte Carlo Simulations and Self-Consistent Field Theory

M. Müller*

Institut für Physik, WA 331, Johannes Gutenberg Universität, D-55099 Mainz, Germany

L. Gonzalez MacDowell

Departimento de Quimica Fisica, Facultad de Ciencias Quimicas, Universidad Complutense, 28040 Madrid, Spain

Received October 25, 1999; Revised Manuscript Received February 22, 2000

ABSTRACT: We investigate the structure and thermodynamics of inhomogeneous polymer solutions in the framework of a coarse-grained off-lattice model. Properties of the liquid−vapor interface and the packing of the solution in contact with an attractive wall are considered. The wall interacts with the monomers via a long-range interaction. We employ Monte Carlo simulations in the grand canonical ensemble and self-consistent field calculations to study segment profiles, excess free energies, and the wetting behavior. The self-consistent field calculations incorporate the detailed chain structure via a partial enumeration scheme and use a weighted−density functional ansatz for the monomeric interactions. Quantitative agreement between the Monte Carlo simulations and the self-consistent field calculations is achieved for the conformational arrangements at the wall. Only qualitative agreement is obtained for the excess free energies of interfaces and surfaces. Possible sources for the quantitative deviations are discussed. Using the Young equation, we accurately locate the first-order wetting transition. In the Monte Carlo simulations and the self-consistent field calculations, we find a strong first-order wetting transition and locate the concomitant prewetting line. The behavior of the prewetting line close to the bulk coexistence yields a compatible estimate for locating the wetting transition. The location of the prewetting critical point is estimated in the simulations.

I. Introduction

The phase behavior and properties of inhomogeneous polymer solutions has attracted abiding interest.[1] The thermodynamic behavior of polymers at a free surface or in contact with a substrate determines the wetting properties and is relevant to many technical applications (e.g., protective coatings, lubrication, adhesives). Controlling the properties at interfaces and surfaces is a promising route for tailoring materials to applications. For instance, the properties of surfaces in chemically heterogeneous polymers depend sensitively on the chemical groups which are exposed at the surface.[2] The chemical subunits, in turn, can be tuned by the polymer architecture and depend on the temperature. Structuring the substrate on a microscopic length scale is another route for modifying the thermodynamical properties.[3]

While surface free energies in polymer solutions are routinely measured experimentally and the wetting behavior of polymer films on substrates is the subject of recent experimental interest, our theoretical understanding of the structure and thermodynamics of homopolymer solutions is still incomplete. The simplest thermodynamic description is based on the Flory−Huggins model[4] of a binary polymer mixture treating the solvent as a short chain length limit of one component. Within this framework,[5,6] the critical density decreases such as $1/\sqrt{N}$ and the critical temperature approaches a constant value with a $1/\sqrt{N}$ correction. The limiting value $T_c(N \to \infty)$ coincides with the Θ temperature at which a single chain collapses from a swollen conformation $R \sim N^{\nu}$ with $\nu = 0.588$ for $T > \Theta$ to a compact globule for $T < \Theta$. Below T_c and for long chains, the density inside the collapsed coil corresponds to the density of the liquid phase at coexistence with the vapor. The Θ point is expected to be tricritical, and mean field theory is correct up to logarithmic corrections. These corrections have been calculated by Duplantier.[7] However, computer simulations[8−11] and experiments[12,13] reveal that the asymptotic behavior is not reached for chain lengths typically accessible in simulations or experiments.

In contrast to the situation in a binary blend of comparable chain lengths,[14,15] the Flory−Huggins parameter χ at the onset of phase separation is of order unity. These strong interactions on the monomer scale are expected to impart a pronounced temperature dependence on the chain conformation and the structure of the polymeric fluid. Of course, this effect is completely absent in the Flory−Huggins lattice approach. Hence, a more quantitative description has to capture simultaneously the effect of chain connectivity and the balance of attractive and repulsive interactions. There are some phenomenological extensions of the mean field theory (e.g., by Sanchez and Lacombe[16]) which try to describe the equation of state in terms of a small number of parameters. More recently, the structure of polymer solutions has been investigated by P−RISM theory. This approach deals with a polymeric version of the Ornstein−Zernike equation and aims at calculating the fluid structure on a microscopic basis. While P−RISM[17] yields a good description of dense multicomponent systems, Chatterjee and Schweizer[18,19] found a rather significant dependence on the details of the relation used to close the Ornstein−Zernike equation. Most notably, not all closure relations yield the same scaling of the critical temperature and density with chain length.[18] Alternative descriptions along the lines of Wertheim's theory[20−24] of associating fluids have been explored. Here, the monomer fluid acts as a reference state and the association of the monomers to form

10.1021/ma991796t CCC: $19.00
Published on Web 04/22/2000

chains is treated perturbatively. It can be shown explicitly that the scaling of the critical point parameters complies with the mean field prediction. Nevertheless, the effect of chain connectivity and structure of the polymer fluid at low densities is not correctly captured by the theory. For instance, the chain length dependence of the second virial coefficient above the Θ temperature is predicted incorrectly.[25]

The properties of inhomogeous polymer solutions have been investigated in density functional studies. [26−28] The relation between the different approaches is, e.g., discussed in refs 27 and 28. Kierlik and Rosinberg[26,27] extended Wertheim's perturbation theory[20] of polymerization to a density functional scheme. Their theory captures the coupling between intramolecular correlations and the density approximatively. It has been applied to study the packing of hard chains against a hard wall. The theory predicts the density profiles at the wall as well as local intrachain correlations (e.g., the orientation of bond vectors). Another density functional theory has been developed by McCoy and coworkers.[28−30] It is based on the work of Chandler, McCoy, and Singer[39] and employs the direct correlation function of the P−RISM theory[17] as an input to predict the packing of chains at a wall. The scheme has been applied to hard chains of various architectures[28,29] close to a wall and has been generalized by Nath et al.[40] to diblock copolymers. The density profile, the distribution of individual segments, and the chain extensions have been investigated. A third version of density functional theory has been explored by Woodward and Yethiraj.[31−35] They use a phenomenological weighted-density functional ansatz for the monomeric interactions. The theory requires an equation of state and a weight function[33] as input. The latter introduces some information about the packing into the theory. The comparison with Monte Carlo simulations shows that a rather simple estimate of the weight function already yields a good prediction for the packing of hard chains at a hard wall. The relation between the weight function and the direct correlation function has been investigated.[34,35] The approach also yields the segment density profiles at a wall and has been compared to a mixtures of monomers and polymers confined into a slitlike pore. This latter approach is very similar to the one adopted by us. However, to the best of our knowledge, all the above theories have been focused on hard chain fluids at a wall, and the effects of attractive intermolecular interactions have not yet been explored in detail.

Calculating interface and surface free energies, however, requires additionally some information about the thermodynamics inside the miscibility gap. For instance, in a simple square gradient type theory[41] the interfacial tension is a functional of the free energy density of a hypothetical homogeneous system inside the coexistence region. In polymer solutions, this formidable task amounts to describing the transition from a gas of collapsed globules to a concentrated solution of Gaussian chains. Of course, homogeneous states in the miscibility gap are not accessible, and there is little guidance from experiments or computer simulations as to how to extrapolate the free energy density from the one-phase region into the coexistence region. Interface profiles and excess free energies provide a rather indirect testing bed for the assumptions. Moreover, the free energy cost of an inhomogeneous concentration profile involves both entropic contributions from the chain connectivity and enthalpic contributions from the finite extension of the interaction potentials. Since the interfacial width is comparable to the monomer scale both contributions are of similar importance. Additionally, the chain architecture on these small length scales might not be describable by a simple coarse-grained chain model (e.g., Gaussian chains). The above arguments show that the quantitative behavior depends strongly on the details of the interactions and chain architecture.

In this paper we use Monte Carlo simulations and self-consistent field calculations to explore the structure and thermodynamics of surfaces and interfaces in polymer solutions. We present a detailed quantitative comparison between the two methods by investigating a variety of structural and thermodynamic quantities for the same model. These include the packing of the monomers at an attractive wall, the orientations of chains and segment profiles at surfaces and interfaces, the surface and interface free energies, and the wetting properties. We achieve only qualitative agreement between Monte Carlo simulations and self-consistent field calculations. The comparison might help one to identify the most important approximations in the self-consistent field treatment. In the next section we describe our bead−spring model and the Monte Carlo technique. The subsequent section outlines our self-consistent field technique and briefly summarizes the bulk thermodynamics as obtained via Wertheim's thermodynamic perturbation theory (TPT1)[20] in our previous work[42] (henceforth referred to as paper I). This equation of state, which we have compared to Monte Carlo simulations,[42] will be employed in the self-consistent field calculations. Section IV compares the results of the Monte Carlo simulations and the self-consistent field theory. We conclude with a discussion of our findings and an outlook on future work.

II. Model and Monte Carlo (MC) Technique

A. An Off-Lattice Model for Polymer Solutions. Being interested in the qualitative features of inhomogeneous polymer solutions we use a coarse-grained off-lattice model which incorporates only the relevant features of polymeric materials: excluded volume of the segments, chain connectivity, and an attractive interaction between monomers which drives the phase separation. Our model is similar in spirit to the bead−spring model of Kremer and Grest.[43] Monomeric units are modeled as Lennard−Jones particles:

$$V_{\mathrm{LJ}}(r) = 4\epsilon\left\{\left(\frac{\sigma}{r}\right)^{12} - \left(\frac{\sigma}{r}\right)^{6}\right\} + \frac{127}{4096} \quad \text{for } r < 2 \times 2^{1/6}\sigma \tag{2.1}$$

The potential is cutoff at twice the minimum distance and shifted so as to produce a continuous potential. The short-range repulsive part models the excluded volume between monomers, whereas the attractive portion results in a liquid−vapor coexistence. In addition to the Lennard−Jones potential, monomers along a chain interact via a FENE potential:

$$V_{\mathrm{FENE}}(r) = -15\epsilon(R_0/\sigma)^2 \ln\left(1 - \frac{r^2}{R_0^2}\right) \quad \text{with } R_0 = 1.5\sigma \tag{2.2}$$

The parameters are chosen such that the Lennard−Jones potential between nonbonded segments prefers a distance $r_{\mathrm{nb}} \approx 1.12\sigma$, while the most favorable distance between bonded neighbors, $r_{\mathrm{b}} \approx 0.96\sigma$, is slightly

smaller. Molecular dynamics simulations of the identical model by Bennemann et al.[44] have shown that the occurrence of two incompatible length scales leads to a density driven glass transition around a monomer number density $\phi \approx 1.0/\sigma^3$ rather than the build up of long-range crystalline order (as it emerges in the corresponding monomer fluid). In the following all length scales are measured in units of the Lennard−Jones length σ, and all energies are measured in units of the parameter ϵ of the Lennard−Jones potential.

While the self-consistent field calculations are not restricted to short chain lengths, the computational expense for equilibrating large scale structures (e.g., wetting layers) in the Monte Carlo simulations increases rapidly with increasing chain length or density. Therefore, we use the chain length $N = 10$ in our simulations. If we were to map a realistic polymer model onto our coarse-grained model, this chain length would correspond to roughly 40 chemical repeat units.[45] An investigation of the chain length behavior of the phase diagram reveals that our very short chains do not reproduce the asymptotic scaling behavior of long macromolecules.[42] However, we expect some qualitative features of polymer solutions to emerge already for the small chain length studied here. For instance, the critical temperature of the polymer solution $T_c(N = 10) = 1.98(3)$ is well above the critical temperature of the monomer fluid $T_c(N = 1) = 1.00(1)$. Most of the data are collected for chain length $N = 10$ and $T = 1.68$. For these parameters, a liquid of monomer number density $\phi = 0.61$ coexists with a vapor of density $\phi = 0.0083$. On one hand, the temperature is low enough such that the vapor pressure over the liquid is nearly zero and the vapor phase has a vanishingly small polymer content. In this regime, the properties do not depend strongly on chain length. For $N = 20$, the coexistence density is $\phi = 0.65$ and the interfacial tension is about a factor 1.57 higher than for $N = 10$. $\gamma_{LV}(N = 10) = 0.0953 k_B T$. On the other hand, the liquid density is low enough as to allow for a reasonable fast equilibration of density fluctuations.

We chose a rectangular box geometry $L \times L \times D$ with $L < D$. Investigating interface properties we impose periodic boundary conditions, such that systems with densities inside the miscibility gap contain two interfaces of size $L \times L$. Studying surface properties we introduce impenetrable and ideally flat walls at $z = 0$ and $z = D$, while applying periodic boundary conditions in the lateral directions. The interaction between monomers and each wall takes the form

$$V_{wall}(\Delta z) = \epsilon_w \left\{ \left(\frac{\sigma}{\Delta z}\right)^9 - f_w \left(\frac{\sigma}{\Delta z}\right)^3 \right\} \qquad (2.3)$$

where Δz denotes the distance between a monomer and the wall. No cutoff is applied, and ϵ_{wall} is measured in units of ϵ. This potential mimics the van der Waals interactions between the molecules of the wall and the monomers. $\epsilon_w f_w$ plays the role of the Hamaker constant. Unless noted otherwise, we choose $f_w = 1$.

B. Monte Carlo (MC) Method. We perform Monte Carlo simulations in the canonical ensemble to study the detailed profiles of a concentrated polymer solution in contact with a wall and the liquid−vapor interface. Random local displacements of the individual segments as well as slithering-snake like motions were used to update the polymer conformations. Typically these MC moves are applied in the ratio 1:1. Every 100 local displacements per monomer and 100 slithering-snake motions per polymer a configuration is stored for further analysis. For each strength of the monomer−wall interaction about 14 000 configurations of size $18 \times 18 \times 36$ were examined. Each configuration contains 6740 or 3600 monomers for investigating a surface in contact with a liquid or interface properties, respectively.

We have attempted to measure the excess free energy of a spatial inhomogeneity via the anisotropy of the pressure.[46−50] Using the virial of the forces on the particles, we define an internal pressure profile according to

$$\frac{p_x(z)}{D} = \frac{k_B T}{V} \sum_{i=1}^{nN} \delta(z - z_i) - \frac{1}{2V} \sum_{i,j<i} \frac{\partial \Phi}{\partial r_{ij}} \frac{x_{ij}^2}{r_{ij}} [\delta(z - z_i) + \delta(z - z_j)] \qquad (2.4)$$

where the sum runs over all particles in the system and Φ denotes the interparticle interactions, i.e., the Lennard−Jones potential between all particles and the FENE potential between bonded neighbors along the chain. z_i denotes the z coordinate of particle i, and r_{ij} denotes the interparticle distance. Similar expressions hold for the lateral components p_y and p_z. In a homogeneous system the pressure is isotropic.

We have applied this virial expression successfully for measuring the equation of state (cf. paper I). If fixed walls are present, the z component of the pressure profile comprises an additional contribution due to the monomer−wall interaction

$$\frac{p_{wall}(z)}{D} = -\frac{1}{V} \sum_i \frac{\partial V_{wall}}{\partial \Delta z} \Delta z \delta(z - z_i) \qquad (2.5)$$

We have applied this equation for the case when the liquid fills the container and there is no liquid−vapor interface. The surface free energy corresponds to a change in the free energy due to a deformation which increases the surface or interface area, but leaves the volume of the system invariant. This yields for the excess free energy[50]

$$2\gamma = \int_0^D dz \left\{ p_z(z) + p_{wall}(z) - \frac{p_x(z) + p_y(z)}{2} \right\} \qquad (2.6)$$

where the integration is extended over the whole system and the factor 2 appears because the system contains two surfaces. A pressure profile at a wall for $T = 1.68$, $\epsilon_w = 4$, and coexistence density is presented in Figure 1. Though the profile contains useful information about how the packing structure of the fluid affects the excess free energy, the contributions of the Lennard−Jones almost exactly cancels the FENE potential contribution. The integral over the z component of the Lennard−Jones pressure yields 275.2 while the anisotropic contribution of the Lennard−Jones potential to the excess free energy amounts only to −3.2. A similar behavior is observed for the contribution of the wall and the FENE potential. An accuracy of about 10% in the surface tension requires the knowledge of the individual pressure contributions to a relative accuracy of 10^{-4}. Therefore, we conclude that at least for this combination of parameters the anisotropy of the pressure is a rather inaccurate measure of the excess free energy. These

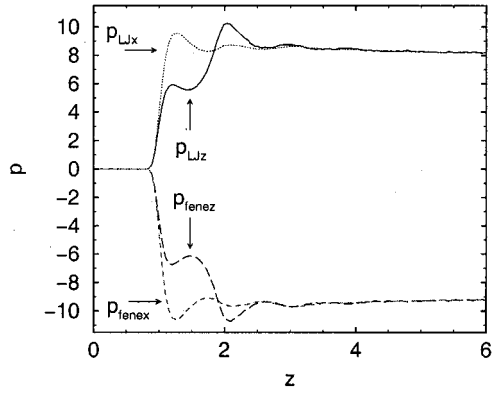

Figure 1. Lateral and perpendicular components of the pressure for the Lennard−Jones interactions and the attractive FENE interactions presented for $T = 1.68$, $\epsilon_w = 4$, $\phi_{av} = 0.578$, and $L = 18$ and $D = 36$.

values also exemplify that the excess free energies result from a very subtle balance between the different interactions, and they provide a sensitive test for predicting the structure of the inhomogeneity. A similar behavior is expected at the liquid−vapor interface.

In view of these difficulties, we have measured the excess free energies of inhomogeneous solutions in the grand canonical ensemble; i.e., rather than simulating at a constant number of particles, we fix the chemical potential μ of the polymer. In addition to the updates of the polymer conformations (as described above), we perform polymer insertions and deletions via configurational bias.[51−53] The configurational bias scheme utilizes a biased insertion method to "grow" a polymer successively into the system. At each step a small number (typically 25) of segment positions is examined and a position for inserting of the next monomer along the chain is chosen according to its Boltzmann weight. This choice bias the insertion toward nonoverlapping/low-energy chain conformations. Once a chain has been grown, the bias in the construction is compensated for in the Monte Carlo lottery. Typically, we used systems of size $13.8 \times 13.8 \times 27.6$ in the grand canonical simulations.

The grand canonical simulation scheme does not correspond to a realistic dynamics. However, it allows for a much faster equilibration of density fluctuations, which would decay in the canonical ensemble via the slow diffusive motion of the polymers. For instance, the equilibration of the thickness of wetting layers at the surface in the canonical ensemble would require an exchange of polymers between the vapor phase and the liquid layer at the wall via polymer diffusion. To act as a particle reservoir, the vapor phase would have to be enormously large to accommodate sufficient polymers to observe the dependence of the wetting layer on the monomer wall interaction.

The probability distribution $P(\phi)$ of the density is monitored in the course of the simulation. At phase coexistence this distribution exhibits two pronounced peaks, which correspond to the vapor and the liquid phase. The coexistence chemical potential $\mu_{coex}(T)$ is fixed by the condition of equal weight in both peaks:[54,55]

$$\int_0^{\phi^*} d\phi\, P(\phi) \stackrel{!}{=} \int_{\phi^*}^{\infty} d\phi\, P(\phi) \quad \text{with } \phi^* = \int_0^{\infty} d\phi\, P(\phi)\phi \tag{2.7}$$

Below the critical temperature, the vapor and the liquid

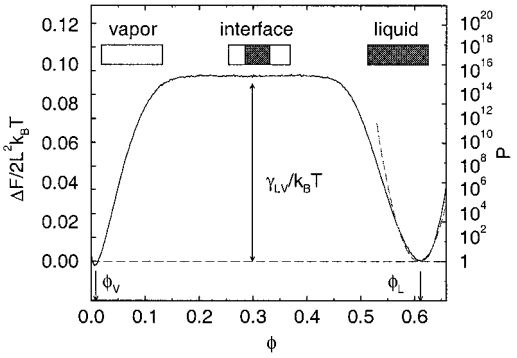

Figure 2. Illustration of the simulation technique for temperature $T = 1.68$ and $\mu_{coex} = 106.897$. A cuboidal system geometry $13.8 \times 13.8 \times 27.6$ with periodic boundary conditions in all three directions is used. The solid line corresponds to the negative logarithm of the probability distribution $P(\phi)$ in the grand canonical ensemble. The two minima correspond to the coexisting phases, and the arrows on the ϕ axis mark their densities. The height of the plateau yields an accurate estimate for the interfacial tension γ_{LV}. The dashed line is a parabolic fit in the vicinity of the liquid phase employed to determine the compressibility. The typical system configurations are sketched schematically.

phase are separated by a large free energy barrier. For systems with periodic boundary conditions in all three directions, the typical configurations at intermediate densities consist of a slab of liquid which is separated by two interfaces of area $L \times L$ from the vapor. The probability of these configurations is suppressed due to the free energy costs of the two interfaces.[56] An example for the free energy $F(\phi) = -k_BT \ln P(\phi)$ is presented in Figure 2. The plateau in the free energy (between the minima) indicates that the two interfaces change their mutual distance (and thereby alter the average density) without free energy cost. Therefore, they do not interact and the excess free energy is indeed the sum of the individual interface contributions $2\gamma L^2$. To overcome the associated free energy barrier in the simulations and to encourage the system to "tunnel" between the two phases we add a term $k_BT \ln W(\phi)$ to the original Hamiltonian.[57] Choosing the reweighting function $W(\phi) \approx P(\phi)$, the system samples all densities with roughly the same probability. A good estimate of the reweighting function is provided by histogram analysis[58] of the results at higher temperatures (though other extrapolation schemes can be envisaged[59]). Thus, a single simulation yields the coexistence value of the chemical potential, the coexistence density, and the interfacial tension.

We apply the same Monte Carlo technique in the presence of two walls.[60] The simulations sample all densities between the vapor phase (V) and the liquid phase (L) in contact with the walls. Again the logarithm of the probability distribution yields the free energy as a function of the density. Figure 3 displays the results for $T = 1.68$ at the bulk coexistence value of the chemical potential. The free energy has two minima corresponding to the vapor in contact with the wall (low density) and the liquid in contact at the wall. The ratio of the probability for finding the system in one of both phases yields the difference in the surface free energies $2L^2(\gamma_{VW} - \gamma_{LW}) = k_BT \ln[P(\phi_L)/P(\phi_V)]$. At intermediate densities the typical conformations consist of a liquid slab at each wall. If the system size is large, the distance between the liquid−vapor interfaces and the wall and their mutual distance becomes large. In this limit, the interfaces do neither interact with the walls nor with

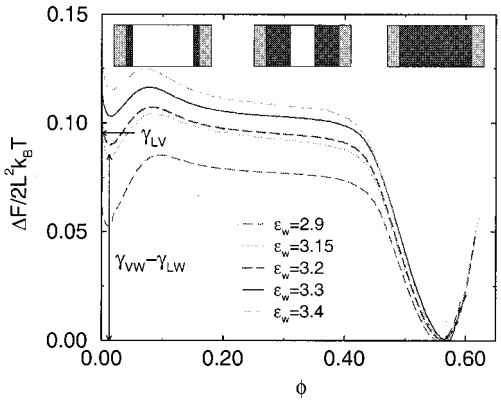

Figure 3. Free energy as a function of the density of a system, which is confined between walls of attractive strength ϵ_w. The grand canonical simulations at $T = 1.68$ and coexistence chemical potential in the bulk are performed in a geometry $13.8 \times 13.8 \times 27.6$. The curves are shifted such that the free energy of the liquid-phase vanishes. The horizontal arrow on the left marks the value of the interfacial tension γ_{LV}, while the vertical arrow marks the difference in the surface tension between the vapor/wall and liquid/wall for $\epsilon_w = 3.15$. Typical system configurations are sketched schematically.

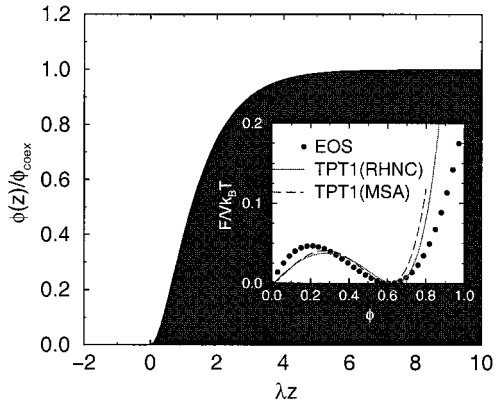

Figure 4. Illustration of the trial profile in the square gradient calculations. The inset compares the free energy density in the square gradient calculation (using the coexistence value of the liquid density and the compressibility of the liquid as determined by the MC simulations) with the TPT1. The solid lines corresponds to the RHNC closure for the monomer liquid; the dashed line shows the result of the MSA closure.

each other, and we expect only a weak dependence of the free energy on the density. In this case, one could try to extract an effective interaction potential between the interface and the wall. The liquid would wet the surface if the plateau value at intermediate densities is lower than the minimum at low densities. However, for the system size studied we do not observe a plateau; i.e., once the interfaces have reached a distance from the wall which is large enough for the effective interaction between the interface and the wall to decay, they already begin to interact mutually. Though our simulation cell is not large enough to extract the effective interface potential (because of the presence of two liquid−vapor interfaces in the simulation box) we can reliably determine $\gamma_{VW} - \gamma_{LW}$. In these limiting states the container is either completely filled with the liquid or the vapor and there are no liquid−vapor interfaces present. The perturbation of the density profile in the liquid extends only over a few σ (cf. Figure 8a), which is much smaller than the extension of the simulation cell.

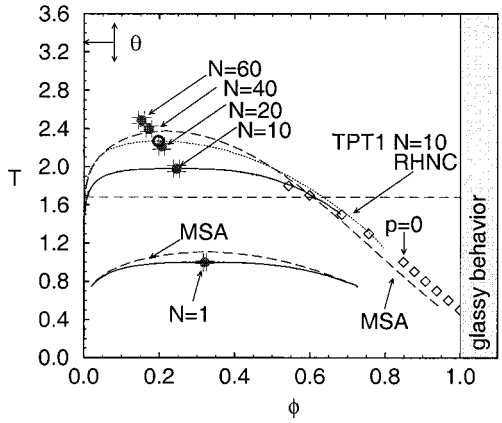

Figure 5. Phase diagram for various chain lengths N. The solid line corresponds to grand canonical MC simulations, while the diamonds refer to canonical simulations at pressure $p = 0$. The dotted lines displays the result of the TPT1 approximation using the RHNC closure for the monomer fluid, the long dashed line represents the TPT1/MSA calculation. The arrow on the temperature axis marks the Θ temperature, and the critical points for larger chain lengths are indicated. The horizontal dashed line marks the temperature $T = 1.68$ at which we investigate the surface and interface properties. The phase diagram of the monomer fluid is also shown. The solid curve refers to the MC simulations, the long dashed line is the result of the integral equation theory using the MSA closure. (Note that the RHNC has no solution close to the critical point of the monomer fluid.)

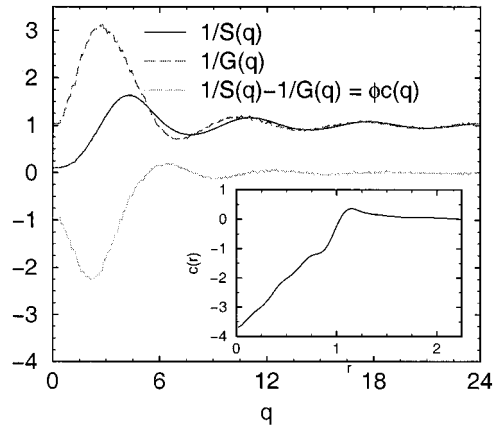

Figure 6. Inverse total structure factor $1/G(q)$, inverse single chain structure factor $1/S(q)$, and Fourier transform of the direct correlation function according to P−RISM theory. The inset displays the direct correlation function in real space. All data are obtained at $T = 1.68$ and $\phi_{coex}^{L} = 0.61$.

Once this free energy difference is calculated for a particular strength of the monomer−wall interaction ϵ_w, the dependence on the attractive strength of the wall can be obtained via thermodynamic integration

$$G(\epsilon_w,\mu) = G(\epsilon_0,\mu) + \int_{\epsilon_0}^{\epsilon_w} d\epsilon_w' \, \frac{\langle E_{wall}(\epsilon_w')\rangle}{\epsilon_w'} \qquad (2.8)$$

where $E_{wall} = L^2 \int dz \, \hat{\phi}(z) V_{wall}(z)$ denotes the interaction energy associated with the monomer−wall interaction potential. However, rather than measuring this wall energy for many different values of the interaction strength ϵ_w, we use an expanded ensemble in which the monomer−wall interaction strength ϵ_w is a Monte Carlo variable.[60] This allows us to calculate the free energy difference between different values of the attractive

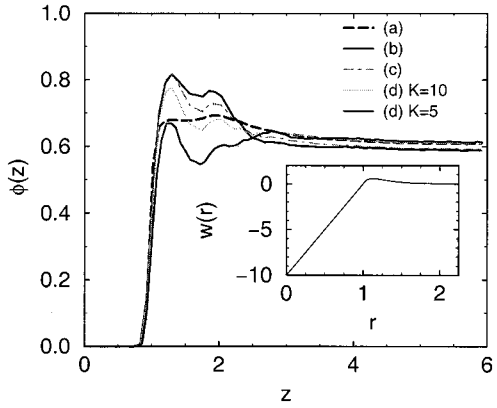

Figure 7. Dependence of the monomer density profile at an attractive wall ($\epsilon_w = 4$) at $T = 1.68$ on the weight function w. The inset shows the weight function ($K = 10$) used in the following calculations. The density profile in the MC simulations and its comparison to the SCF calculation is shown in Figure 8a.

strength ϵ_w in a single simulation run. The partition function of the expanded ensemble takes the form

$$Z \sim \sum_{\{\epsilon_w\}} W_w^{-1}(\epsilon_w)(-G(\epsilon_w)/k_B T) \tag{2.9}$$

where the reweighting factor W_w is adjusted as to achieve uniform sampling of the different ϵ_w values. Initial estimates for the reweighting factor have been obtained via eq 2.8. The Monte Carlo simulation comprises additionally moves which switch between neighboring values of the monomer−wall interactions. (Care has to be exerted at the limiting values to fulfill detailed balance.) Let $P_w(\epsilon_w)$ denote the probability with which the fluctuating wall strength takes the value ϵ_w. Then the difference in the surface free energy of the liquid phase is given by

$$\gamma_{LW}(\epsilon_w) = \gamma_{LW}(\epsilon_0) - \frac{k_B T}{2L^2} \ln\left(\frac{P_w(\epsilon_w)W_w(\epsilon_w)}{P_w(\epsilon_0)W_w(\epsilon_0)}\right) \tag{2.10}$$

where the simulations are performed at the coexistence value of the chemical potential and the system is in the liquid phase. If the system is in the vapor phase, the expression yields the surface free energy difference of the vapor. This is a computationally efficient method for calculating the dependence of the surface free energy on the attractive strength of the interactions if neither the liquid nor the vapor wets the surface completely. For large attraction ϵ_w, the liquid wets the surface and the simulation in the vapor phase becomes metastable (the simulation cell eventually fills with the liquid phase). In the case of a first-order wetting transition, however, the metastable states are well observable in the simulations up to the wetting spinodal. For a very small interaction strength, the vapor wets the wall and the simulation in the liquid-phase becomes metastable, respectively. At this drying transition the difference $\gamma_{VW} - \gamma_{LW}$ equals $-\gamma_{LW}$. The knowledge of the absolute value of $\gamma_{VW} - \gamma_{LW}$ at the drying transition can actually be used as an alternative starting value for the thermodynamic integration,[61] because the transition shows little metastability (cf. below).

III. Self-Consistent Field (SCF) Calculations

A. A Simple Sketch of Surface and Interface Properties. In this section, we briefly sketch some salient features of inhomogeneous polymer solutions in the framework of a Cahn−Hilliard type approach.[41] On this qualitative level, the free energy of an inhomogeneous system comprises two contributions. One stems from the free energy density of the homogeneous system; the other describes the free energy cost of a spatial variation in the density.[62,63]

We assume the free energy density to be a polynomial in the monomer density ϕ

$$\frac{F_{EOS}}{V k_B T} = \frac{1}{2}\zeta\phi(\phi - \phi_{coex}^L)^2 \tag{3.1}$$

where we have expressed the coefficient in terms of the coexistence density of the liquid ϕ_{coex}^L and the compressibility of the liquid ζ. A density independent value of ζ reproduces the cubic dependence of the pressure on the density in a concentrated solution. Moreover, it is the simplest functional form to extrapolate the free energy density around the density of the liquid phase into the miscibility region. We have neglected the translational entropy of the polymers (ideal gas term), which is down by a factor of $1/N$, such that the liquid coexists with a vapor of zero density. This appears to be a reasonable approximation for temperature not too close to the Θ point. Moreover, any conformational contributions to the free energy density of the homogeneous system have been omitted. The free energy density is shown in Figure 4, where we have used the parameters appropriate for $T = 1.68$. A comparison with the quantitative prediction (cf. next section) reveals that the third-order equation of state captures the qualitative features of the free energy density but fails to provide a quantitative description.

The free energy cost of an inhomogeneous density distribution takes a square gradient form

$$\frac{F_{grad}}{k_B T} = \frac{b^2}{24}\int \mathrm{d}^3\mathbf{r}\frac{(\nabla\phi)^2}{\phi} \tag{3.2}$$

where we have used the Lifshitz entropy formula[64] for the conformational entropy costs of a density profile in the long chain length limit. b denotes the statistical segment length. In addition, there is a similar square gradient contribution due to the finite spatial extent of the monomer−monomer interactions. To a first approximation this might be accounted for by a change in b.

The equilibrium profile minimizes the sum of both contributions. Variation of the total free energy with respect to the density profile leads to an Euler−Lagrange equation which is rather difficult to solve analytically.[62] To discuss the basic qualitative features, we simply minimize the free energy with respect to a trial function

$$\phi(z) = \phi_{coex}^L[1 - \exp(-\lambda z)]^2 \quad \text{for } z > 0 \text{ and } 0 \text{ otherwise} \tag{3.3}$$

where we treat the inverse interfacial width λ as a variational parameter. The shape of the trial function is illustrated in Figure 4. This ansatz yields for the individual free energy contributions

$$\frac{F_{EOS}}{A k_B T} = \frac{13\zeta\phi_{coex}^{L3}}{120\lambda} \text{ and } \frac{F_{grad}}{A k_B T} = \frac{b^2}{12}\lambda\phi_{coex}^L \tag{3.4}$$

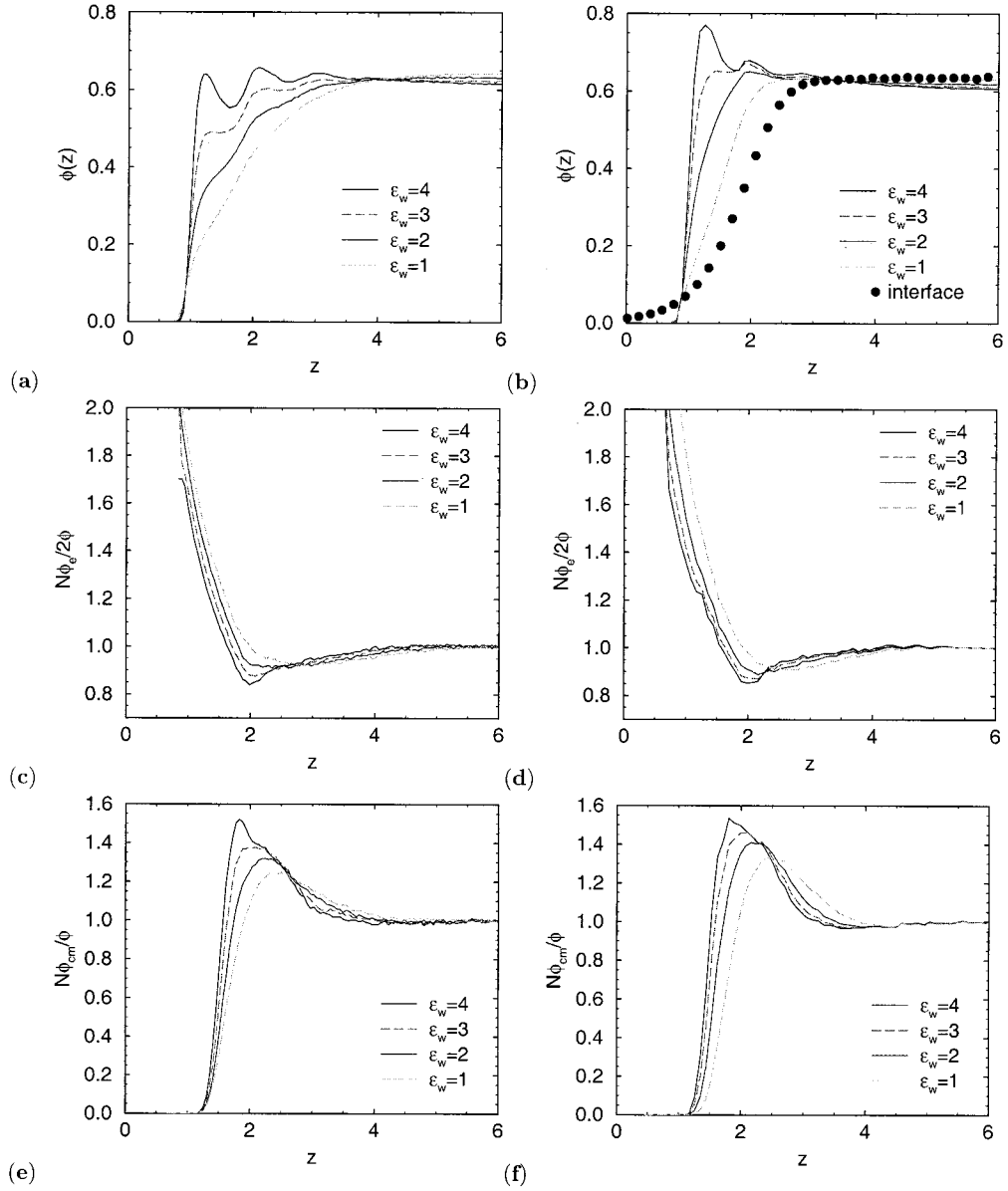

Figure 8. Segments profiles as a function of the monomer−wall interaction ϵ_w. The left column (a, c, e) corresponds to the Monte Carlo simulations; the right column (b, d, f) shows the results of the SCF calculation with $K = 10$. Parts a and b present the packing structure of the total monomer density at the wall for $\epsilon_w = 4$, 3, 2, and 1 from above to below. Parts c and d display the relative density of chain ends at the surface, while parts e and f show the relative density of the center of mass.

The free energy is minimized by the value

$$\frac{1}{\lambda^*} = \frac{b}{\phi_{\text{coex}}^{\text{L}}}\sqrt{\frac{10}{13\zeta}} \tag{3.5}$$

Hence, the interfacial width of a liquid−vapor interface is on the order of the statistical segment length, independent of the chain length, and decreases with temperature. The interface free energy takes the form

$$\frac{\gamma_{\text{LV}}}{k_{\text{B}}T} \equiv \frac{F_{\text{EOS}^*} + F_{\text{grad}^*}}{Ak_{\text{B}}T} = b\phi_{\text{coex}}^{\text{L}2}\sqrt{\frac{13\zeta}{360}} \tag{3.6}$$

These simple calculations are in accord with scaling considerations. The width of an interface between a concentrated solution and its vapor is proportional to the correlation length ξ which scales as $\xi \sim 1/\phi_{\text{coex}}^{\text{L}}$. Moreover, the scale of the interfacial tension is set by $k_{\text{B}}T/\xi^2$.[65]

In the framework of the variational treatment, the density vanishes at a finite distance from the center of the interface. Hence, at phase coexistence with the vapor, the surface tension of the liquid at a hard wall equals the interfacial tension. Generally,[66] this value is an upper bound, because the vapor would wet the wall otherwise. This approximation corresponds to a drying transition at $\epsilon_w = 0$. If the wall interacts with the monomers, the surface free energy is given by eq 2.8. To a first approximation we can describe the density at a wall by a stepwise profile $\phi(z) = \phi_{\text{coex}}^{\text{L}}\Theta(z - f_w^{-1/6})$ and obtain for the surface free energy:

$$\gamma_{\text{WL}} \sim \gamma_{\text{LV}} - f_w^{4/3}\frac{3\epsilon_w\phi_{\text{coex}}^{\text{L}}\sigma}{8} \tag{3.7}$$

At small values of ϵ_w this assumption overestimates the density close to the wall, and the surface free energy will decrease not as rapidly as predicted by the above

equation. At large values of ϵ_w, the density at the wall exceeds the density in the bulk. The density of the vapor which coexists with the liquid is zero, and a possible enrichment of the liquid at the wall is neglected. Therefore, we approximate the surface tension of the vapor by $\gamma_{VW} \approx 0$.

Using the Young equation,[67] we can estimate the strength of the monomer−wall interaction ϵ_w^{wet} at which the polymer liquid wets the surface. If the vapor pressure of the polymer is vanishingly small $\gamma_{VW} \approx 0$ and $\gamma_{LW}(\epsilon_w = 0) \approx \gamma_{LV}$. Hence, the attractive interactions between the monomers and the wall have to compensate twice the liquid−vapor interfacial tension. Using eqs 3.6 and 3.7 we obtain

$$f_w^{4/3}\frac{\epsilon_w^{wet}}{k_B T} = \frac{b\phi_{coex}}{\sigma}\sqrt{\frac{416}{405}\zeta} \tag{3.8}$$

Within this approximation, the wetting transition is first order, and there is no qualitative difference between long-range and short-range interactions (except for the numerical constants). Moreover, the wetting transition temperature is independent of the chain length.

B. TPT1: an Approximation for the Thermodynamics of the Homogeneous System. Using the monomer fluid of Lennard−Jones particles as a reference system, we have determined the free energy of the polymer solution by calculating the effect of the bonding potential V_{FENE} as a thermodynamic perturbation in paper I.[42] For completeness we briefly summarize the salient features. The free energy difference between the polymer solution and the monomeric reference system (LJ) is given by

$$\frac{F - F_{LJ}}{k_B T} = -\ln\frac{\left[\frac{1}{(n)!}\int D[\mathbf{r}]\exp\left(-\frac{E_{LJ}[\mathbf{r}] + E_{FENE}[\mathbf{r}]}{k_B T}\right)\right]}{\left[\frac{1}{(nN)!}\int D[\mathbf{r}]\exp\left(-\frac{E_{LJ}[\mathbf{r}]}{k_B T}\right)\right]}$$

$$= -\ln\frac{(nN)!}{n!} - \ln\left\langle\exp\left(-\frac{E_{FENE}[\mathbf{r}]}{k_B T}\right)\right\rangle_{LJ} \tag{3.9}$$

where $E_{LJ}[\mathbf{r}]$ denotes the sum over all Lennard−Jones interactions, and $E_{FENE}[\mathbf{r}]$ represents the sum over the $n(N-1)$ bonding potentials. To first order, the last term can be approximated in the form (TPT1):[20−24]

$$\left\langle\exp\left(-\frac{E_{FENE}[\mathbf{r}]}{k_B T}\right)\right\rangle_{LJ} \approx \left[\frac{1}{V}\int \mathrm{d}^3\mathbf{r}_{12}\, g_{LJ}(\mathbf{r}_{12})\exp\left(-\frac{V_{FENE}(\mathbf{r}_{12})}{k_B T}\right)\right]^{n(N-1)} \equiv \left[\frac{\delta}{V}\right]^{n(N-1)} \tag{3.10}$$

This approximation results in the following relation between the free energy density of the Lennard−Jones monomer fluid and the polymer solution

$$\frac{F}{Vk_B T} = \frac{F_{LJ}}{Vk_B T} + \frac{\phi}{N}\ln\frac{\phi}{N} - \phi\ln\phi - \phi\left(1 - \frac{1}{N}\right)\ln\delta \tag{3.11}$$

In principle, we could determine the pair correlation function $g_{LJ}(\mathbf{r}_{12})$ of the Lennard−Jones reference fluid in a separate MC simulation. However, the SCF calculations require the knowledge of the g_{LJ} for many different densities and temperatures. Moreover, the bonded distance is smaller than the typical distance between Lennard−Jones particles such that we would have to generate very accurate data for g_{LJ} at small interparticle distances for the evaluation of the above integral. We rather determined the structure and the thermodynamics of the reference system from an integral equation approach. Two closures to the Ornstein−Zernike equations of the reference system have been considered: the mean spherical approximation (MSA) and the reference hypernetted chain closure (RHNC). Both closures yield quite similar results. This information was then used to calculate the bulk thermodynamics of the polymer system. The results of TPT1 for the equation of state and the phase diagram were compared to Monte Carlo results. Good qualitative agreement between TPT1 and MC was achieved without any adjustable parameter. Also the scaling of the critical point parameters with chain length was investigated. TPT1 agrees with the scaling predictions of the Flory−Huggins model in the long chain length limit and captures qualitatively some of the deviations observed in simulations of short chains. The reader is referred to paper I for further details.[42] The phase diagram of the Lennard−Jones fluid and the polymer solution of chain length $N = 10$ is presented in Figure 5. At low temperatures, the RHNC closure gives a slightly better result for the density of the liquid than the MSA closure. Therefore, we use the RHNC results for our calculations unless noted otherwise. The applicability of TPT1 is mainly limited by two conditions: (a) Being a mean field theory, density fluctuations are not properly accounted for and TPT1 overestimates the critical temperature of the polymer fluid. (b) The perturbative treatment of the effect of the bonding potential is poor if the structure of the Lennard−Jones reference fluid differs strongly from the structure of the polymer solution. In the concentrated regime the fluid structure is determined by the density and is only weakly perturbed by the bonding potential. Hence, TPT1 gives a good description. Note, however, that in our model the bonding potential favors a slightly shorter particle distance than the Lennard−Jones potential between nonbonded particles. Therefore, our model is not particularly chosen for applying TPT1.[24] Additionally, close to the critical point of the reference fluid [$T_c(N = 1) \approx 1$] and at low densities, the structures of the monomer and polymer fluids differ strongly. One expects that TPT1 performs less well at low temperatures, where a concentrated phase coexists with a dilute solution. Moreover, it does not predict the density dependence of the polymer structure nor does it properly distinguish between inter- and intramolecular interactions. In summary, the validity of the TPT1 approximation for investigating the liquid−vapor coexistence is limited to the rather narrow regime $T_c(N) \gg T \gg T_c(N = 1)$. However, it also gives a good description (far) above the critical temperature $T_c(N)$ as shown in paper I.[42]

Despite all these caveats, TPT1 yields for our model a good description of the binodals (not too close to the critical point) and the equation of state without any adjustable parameter. Most important, it provides the

free energy also for the unstable homogeneous state inside the miscibility gap without any ad hoc extrapolation procedure. The latter information is required by the self-consistent field calculations, and therefore we have decided to use the TPT1 results as an input.

C. Self-Consistent Field (SCF) Technique. Our self-consistent field approach is similar to the density functional method by Yethiraj/Woodward[31,33] and McCoy and co-workers.[28] The starting point is the canonical partition function Z of n polymers in a volume V

$$Z \sim \frac{1}{n!} \int D[\mathbf{r}] P[\mathbf{r}] \exp\left(-\frac{F_0[\hat{\phi}(\mathbf{r})]}{k_B T}\right) \quad (3.12)$$

where $\hat{\phi}$ denotes the monomer density

$$\hat{\phi}(\mathbf{r}) = \sum_{i=1}^{n} \sum_{i_m=1}^{N} \delta(\mathbf{r} - \mathbf{r}_{i,i_m}) \quad (3.13)$$

The second sum runs over all N monomers of a chain. $\mathbf{r}_{i,i_m}$ denotes the coordinate of the i_mth monomer of chain i. $D[\mathbf{r}]$ sums over all polymer conformations, and $P[\mathbf{r}]$ denotes the probability distribution of noninteracting chain conformations. This factor incorporates also the effect of short range intramolecular interactions, which determine the shape of the polymer in the homogeneous system. F_0 denotes the free energy due to intermolecular interactions and long-range intramolecular interactions. At this stage, we neglect any coupling between the chain conformations and the thermodynamic state of the system. Our calculations reproduce the chain conformations characteristic of the concentrated solution which coexists with the vapor phase at temperature $T = 1.68$. This is a quite drastic assumption, because the polymer conformations change from a collapsed globule at low polymer concentration to a random walk in the concentrated solution (cf. paper I). However, the free energy (of the isolated globule and the liquid) below the Θ temperature is chiefly determined by the balance between attractive and repulsive contributions to the monomer−monomer interaction; the conformational entropy appears not to dominate the behavior.

We make a weighted-density functional ansatz for the monomer−monomer interaction F_0:[31,32,68]

$$\frac{F_0[\phi(\mathbf{r})]}{k_B T} = \int d^3\mathbf{r}\, \phi(\mathbf{r}) g(\bar{\phi}(\mathbf{r}))$$

$$\text{with } \bar{\phi}(\mathbf{r}) = \int d^3\mathbf{r}'\, w(\mathbf{r} - \mathbf{r}')\phi(\mathbf{r}') \text{ and } \int d^3\mathbf{r}\, w(\mathbf{r}) = 1 \quad (3.14)$$

Phenomenologically, the weight function w parametrizes the spatial extension of the monomer−monomer interaction, while the free energy density g describes the thermodynamics of the homogeneous system. The derivation of a mean field approximation to the partition function (eq 3.12) follows the lines of self-consistent field calculations[69−74] in polymer systems. Introducing auxiliary fields U and Φ, we can rewrite the multichain partition function in terms of noninteracting chains:

$$Z \sim \int DUD\Phi \exp\left(-n \ln n - \frac{F_0[\hat{\phi}(\mathbf{r})]}{k_B T} + \int d^3\mathbf{r}\, U(\mathbf{r})\Phi(\mathbf{r}) + n \ln QV\right) \equiv$$

$$\int DUD\Phi \exp\left(-\frac{F[U,\Phi]}{k_B T}\right)$$

$$\text{with } \frac{F[U,\Phi]}{Vk_B T} = \frac{\phi_{av}}{N} \ln \frac{\phi_{av}}{N} + \frac{F_0[\hat{\phi}(\mathbf{r})]}{Vk_B T} - \frac{1}{V}\int d^3\mathbf{r}\, U(\mathbf{r})\Phi(\mathbf{r}) - \frac{\phi_{av}}{N} \ln Q[U] \quad (3.15)$$

$Q[U]$ denotes the single chain partition function in the external field U.

$$Q[U] = \frac{1}{V}\int D_1[\mathbf{r}] P_1[\mathbf{r}] \exp(-\int d^3\mathbf{r}'\, U(\mathbf{r}')\hat{\phi}_1(\mathbf{r}')) \quad (3.16)$$

and $\phi_{av} = nN/V$ is the average monomer density. The functional integral (eq 3.15) cannot be evaluated explicitely, and we resorted to a saddle point approximation. At this stage, fluctuations of the local density are neglected. The values of the field U and the density Φ which minimize the free energy functional F are denoted by lower case letters:

$$u(\mathbf{r}) \frac{D}{D\Phi} \frac{F_0[\hat{\phi}(\mathbf{r})]}{k_B T} = g(\bar{\phi}(\mathbf{r})) + \int d^3\mathbf{r}'\, w(\mathbf{r} - \mathbf{r}')\phi(\mathbf{r}') \frac{dg}{d\phi}(\mathbf{r}')$$

$$\phi(\mathbf{r}) = -\frac{\phi_{av} V}{N} \frac{D}{DU} \ln Q[U] = \frac{\phi_{av} V}{N} \frac{\int D_1[\mathbf{r}] P_1[\mathbf{r}] \hat{\phi}_1(\mathbf{r}') \exp(-\int d^3\mathbf{r}'\, u(\mathbf{r}')\hat{\phi}_1(\mathbf{r}'))}{\int D_1[\mathbf{r}] P_1[\mathbf{r}] \exp(-\int d^3\mathbf{r}'\, u(\mathbf{r}')\hat{\phi}_1(\mathbf{r}'))} \quad (3.17)$$

This identifies ϕ as the Boltzmann average of the single chain density in the external field u. To obtain the free energy F we substitute the saddle point values of the field w and the density ϕ into eq 3.15 $F = F[\phi,u]$.

$$\frac{F}{Vk_B T} = \frac{\phi_{av}}{N} \ln \frac{\phi_{av}}{N} - \frac{\phi_{av}}{N} \ln Q[u] - \frac{1}{V}\int d^3\mathbf{r}\, d^3\mathbf{r}'\, w(\mathbf{r} - \mathbf{r}') \frac{d\bar{\phi}}{dg} \phi(\mathbf{r})\phi(\mathbf{r}') \quad (3.18)$$

The sum $D_1[\mathbf{r}]P_1[\mathbf{r}]$ over the single chain conformations is approximated by a partial enumeration over a large number of chain conformations.[15,60,75−79] These were extracted from the simulations of a homogeneous system at temperature $T = 1.68$ and density $\phi = 0.61$. Typically 10^6−10^7 single chain conformations have been employed for the calculations. The enumerations are performed in parallel on a CRAY T3E assigning a small fraction of the conformations to each processor. The spatial dependence of the above equations (eqs 3.16, 3.17, and 3.18) is discretized in terms of the real space coordinate perpendicular to the interface/surface. The corresponding set of nonlinear equations is solved via a Newton−Raphson-like scheme.

Table 1. Parameters of the Equation of State Extracted from TPT1[a]

T	*A*	*B*	*C*	*D*	*E*
1.1	−4.10551	2.15298	12.6369	−30.5381	18.9154
1.15	−3.85618	2.41505	9.17524	−24.3558	15.7369
1.2	−3.62808	2.53448	6.6562	−19.6962	13.3296
1.25	−3.41467	2.53908	4.86261	−16.1983	11.5069
1.3	−3.21799	2.48306	3.55744	−13.5125	10.0971
1.35	−3.04164	2.41371	2.5558	−11.3765	8.97411
1.4	−2.88193	2.33562	1.78831	−9.66594	8.07234
1.45	−2.73553	2.25274	1.19922	−8.28292	7.3407
1.5	−2.6053	2.19384	0.68362	−7.08083	6.70931
1.55	−2.47406	2.0762	0.417926	−6.23648	6.24606
1.6	−2.3649	2.03431	0.0592262	−5.35723	5.7853
1.65	−2.25041	1.93603	−0.103603	−4.73901	5.44249
1.68	−2.19006	1.90194	−0.223643	−4.37135	5.24513
1.7	−2.15291	1.8925	−0.327523	−4.10608	5.10657
1.75	−2.05609	1.83216	−0.469167	−3.59395	4.8267
1.8	−1.96067	1.75298	−0.516702	−3.22056	4.61194
1.85	−1.87789	1.73257	−0.681273	−2.73706	4.35573
1.9	−1.78886	1.6597	−0.686336	−2.45233	4.18612
1.95	−1.71595	1.66021	−0.839751	−2.0257	3.96306
2	−1.63504	1.61004	−0.856124	−1.76005	3.80762
2.05	−1.55402	1.54857	−0.824139	−1.56343	3.684
2.1	−1.48837	1.5575	−0.939084	−1.22107	3.5039
2.15	−1.41309	1.51544	−0.927973	−1.0207	3.38226
2.2	−1.34404	1.492	−0.936948	−0.815764	3.26275
2.24	−1.29652	1.51702	−1.0494	−0.53673	3.11963
2.25	−1.27344	1.46304	−0.93332	−0.624923	3.14844
2.26	−1.26499	1.48562	−0.995521	−0.522021	3.10027
2.265	−1.255	1.46653	−0.955609	−0.547016	3.1071
2.268	−1.25816	1.50311	−1.04555	−0.437471	3.06013
2.269	−1.24497	1.44034	−0.898376	−0.593714	3.12313
2.27	−1.24826	1.46332	−0.951374	−0.53446	3.09895
2.3	−1.21039	1.46787	−0.996615	−0.371677	3.01105

[a] $p = T/N\phi + A(T)\phi^2 + 2B(T)\phi^3 + 3C(T)\phi^4 + 4D(T)\phi^5 + 5E(T)\phi^6$, where the pressure p is measured in units of ϵ/σ^3 and the monomer number density ϕ in units σ^{-3}.

In a spatially homogeneous system the free energy takes the form

$$\frac{F_{\text{hom}}}{Vk_{\text{B}}T} = \frac{\phi}{N}\ln\frac{\phi}{N} - \frac{\phi}{N}\ln Q_0 + \phi g(\phi) \qquad (3.19)$$

where $Q_0 = \int D_1[\mathbf{r}]P_1[\mathbf{r}]$ denotes the constant partition function of an isolated chain. The properties of the spatially homogeneous system are independent of the weight function w, and the equation of state is given by

$$\frac{p}{T} = \phi\frac{\partial}{\partial\phi}\frac{F_{\text{hom}}}{Vk_{\text{B}}T} - \frac{F_{\text{hom}}}{Vk_{\text{B}}T} = \frac{\phi}{N} + \phi^2\frac{\partial g}{\partial\phi} \qquad (3.20)$$

We chose the free energy density $\phi g(\phi)$ such that the thermodynamics of the homogeneous systems in the SCF calculations coincide with TPT1:

$$\phi g(\phi) = \frac{f_{\text{LJ}}^{\text{ex}}}{k_{\text{B}}T} - \phi\left(1 - \frac{1}{N}\right)\ln\delta \qquad (3.21)$$

where $f_{\text{LJ}}^{\text{ex}}$ is the excess free energy of the Lennard−Jones reference system. In practice, we expanded the free energy density g in the equation of state (eq 3.20) in powers of the density up to fifth order and matched the coefficients with the numerical results of the TPT1. The temperature-dependent coefficients were compiled in Table 1. A density-independent term in g is irrelevant to our calculations.

The proper choice of the weight function w is more delicate. Physically, it parametrizes the packing structure on the monomer scale. The density functional work by McCoy and co-workers is also based on a density functional ansatz for the monomer−monomer interactions. Expanding the free energy density g around a reference density ϕ_0, i.e., $g(\phi) = g_0 + g_1(\phi - \phi_0) + ...$ and neglecting any explicite density dependence of w, we can cast our equations in the form

$$\frac{F_0}{Vk_{\text{B}}T} \approx \int \mathrm{d}^3\mathbf{r}\,\mathrm{d}^3\mathbf{r}'\,[\phi(\mathbf{r}) - \phi_0]\,g_1 w(\mathbf{r} - \mathbf{r}')\,[\phi(\mathbf{r}') - \phi_0] + \text{linear terms in } \phi_{\text{av}}$$

$$\text{and } u(\mathbf{r}) \approx \int \mathrm{d}^3\mathbf{r}'\,2g_1 w(\mathbf{r} - \mathbf{r}')\,[\phi(\mathbf{r}') - \phi_0] \qquad (3.22)$$

A comparison with the density functional work of McCoy et al.[28−30] shows that the combination $2g_1 w(\mathbf{r})$ plays a role similar to the direct correlation function $c(\mathbf{r})$. The latter could, in principle, be calculated in the P−RISM framework[17] or be extracted from the MC simulations. This identification is also consistent with the more general relation between the direct correlation function and the weight function derived by Yethiraj and Woodward,[34,35] which does not rely upon an expansion of g in the density and does not omit a density dependence of the weight function.

To get a qualitative estimate for the shape of the weight function we have measured the single chain structure factor $S(\mathbf{q})$ and the total structure $G(\mathbf{q})$ at $T = 1.68$ and the coexistence density $\phi = 0.611$. The results are presented in Figure 6. The collective structure factor of the concentrated solution resembles the melt behavior. It exhibits an "amorphous halo" at about $q = 7$, and the compressibility sum rule yields $G(\mathbf{q} \to 0) = V\langle\Delta\phi^2\rangle/\langle\phi\rangle \approx 1.04$. The P−RISM equation[17] of Schweizer and Curro

$$\phi_{\text{av}}\hat{c}(\mathbf{q}) = \frac{1}{S(\mathbf{q})} - \frac{1}{G(\mathbf{q})} \qquad (3.23)$$

relates the accessible structure factors to the Fourier transform of the direct correlation function, and an inverse transform yields the real space dependence. The result of this procedure is show in the inset of Figure 6. The shape of the direct correlation function in a concentrated solutions resembles qualitatively its analogon in a monomer fluid at the same density. However, there are quantitative deviations, because $c(\mathbf{r})$ does not include intramolecular interactions and the fluid structure of the polymeric system differs slightly from the Lennard−Jones monomer fluid.

The direct correlation function depends (presumably) on density, but we cannot use the procedure described above inside the coexistence region. Therefore, we have decided to treat the weight function as adjustable and to study the consequences of different shapes. Specifically, we have investigated the following choices:

$$w(\mathbf{r}) \sim \delta(\mathbf{r}) \qquad \text{(a)}$$

$$w(\mathbf{r}) \sim \frac{3}{4\pi\sigma^3}\Theta(\sigma - |\mathbf{r}|) \qquad \text{(b)}$$

$$w(\mathbf{r}) \sim (1 - |\mathbf{r}|)\Theta(|\mathbf{r}| - \sigma) \qquad \text{(c)}$$

$$w(\mathbf{r}) \sim \begin{cases} -K(\sigma - |\mathbf{r}|) \text{ for } |\mathbf{r}| < \sigma \\ -\dfrac{V_{\text{LJ}}(\mathbf{r})}{k_{\text{B}}T} \text{ for } |\mathbf{r}| > \sigma \end{cases} \qquad \text{(d)} \qquad (3.24)$$

Since we consider only one-dimensional profiles, we replace integrals of the form $\int d^3\mathbf{r}\ w(\mathbf{r})\phi(\mathbf{r})$ by $\int dz\ w_z(z)\phi(z)$ with

$$w_z(z) = 2\pi \int_0^\infty d\rho\ \rho w(\sqrt{z^2 + \rho^2}) \qquad (3.25)$$

The effect of the weight function is illustrated for the packing at an attractive wall $\epsilon_w = 4$ and $T = 1.68$ in Figure 7. Case a corresponds to a local density functional. Packing effects are completely absent, except for the small correlations mediated by the explicite chain structure. However, the universal polymeric features (i.e., the depletion at the wall) are preserved. This weight function is a common choice in self-consistent field calculation[38,74] for dense multicomponent systems. Choice b has been used in the density functional work of Woodward and Yethiraj[31−34] for tangent hard spheres. It represents the packing of hard particles at wall rather faithfully. However, for our model with repulsive and attractive interactions, this choice overestimates the packing at the wall. The other choices (c and d) are motivated by the general shape of the direct correlation function at high density. Choice c resembles the direct correlations in a hard chain fluid and gives results rather similar to those of case b. This has also been observed by in the work of Yethiraj.[35] Version d tries to incorporate the effect of attraction at least qualitatively. Since the short-range part of the potential is repulsive and the portion further out is attractive, the monomers lose attractive interactions at the wall. Hence, we expect the density at the wall to be lower than for a hard chain fluid. The parameter K determines the relative weight of the attraction for $r > \sigma$ and the repulsion for $r < \sigma$. $K \to \infty$ corresponds to choice c, because the weight function is normalized. Indeed, when K is decreased, the density in the first peak of the monomer profile close to the wall decreases. However, upon decreasing the parameter K, the second peak loses its shape, and we do not achieve quantitative agreement with the profile extracted from the MC simulations for any value of K. $K = 10$ matches the MC data most closely, and we therefore adopt this choice for the SCF calculations unless stated otherwise. Clearly the packing of a fluid with attractive interactions is a difficult problem, because the attractive forces on a particle do not average out in an inhomogeneous system,[80,81] i.e., at a wall or an interface. Our crude treatment captures only the qualitative features, and more sophisticated approaches have been explored for monomeric systems.[81]

Our self-consistent field calculations are similar to the Monte Carlo density functional theory of Yethiraj and Woodward.[34,35] However, we apply the scheme to a system with repulsive *and* attractive contributions to both the monomer−monomer and the monomer−wall interactions. We not only calculate profiles but also investigate excess free energies associated with inhomogeneous density profiles. Moreover, we calculate the density via the Boltzmann average over a large sample of single chain conformations extracted from a concentrated liquid placed into an external potential $u(\mathbf{r})$, rather than performing a single chain MC simulation with the full intramolecular potential and the external field. Besides the computational ease with which such an enumeration can be performed on a parallel computer, the strong intramolecular attractions below the Θ point would actually lead to collapsed chain conformations in a single chain Monte Carlo simulation. This reproduces the correct low-density behavior[34,35] but is inappropriate in the liquid.

Table 2. System Parameters at $T = 1.68$: $b = 1.22$, $1/V\langle(\phi - \langle\phi\rangle)^2\rangle = 1.7$, and $\mu_{coex}^{MC} = 59.228 + 48.669MC$[a]

	ϕ_{coex}^L	ϕ_{coex}^L	γ_{LV}/k_BT	ϵ_w^{wet}
MC	0.611	0.0083	0.0953	3.22
SCF(RHNC)	0.643	0.0015	0.082	1.98
SCF(MSA)	0.606	0.0024	0.081	
EOS			0.144	2.12

[a] MC refers to the Monte Carlo simulations in the grand canonical ensemble. SCF(RHNC) denotes the result of the SCF calculations using the TPT1 approximation. The structure of the reference fluid has been calculated by the Ornstein−Zernike equation with the RHNC closure. While SCF(MSA) refers to the TPT1 approximation in junction with the MSA closure for the monomer fluid, EOS represents the result of the square gradient theory, with a cubic equation of state fitted to the liquid properties.

IV. Comparison between MC Results and SCF Calculations

We compare our MC simulations with the SCF calculations at the temperature $T = 1.68$. At this temperature, the system is well segregated into a very dilute vapor phase and a concentrated solution. Various quantities for the homogeneous system are summarized in Table 2. First, we analyze the structure of the liquid at a wall as a function of the attractive strength ϵ_w, then we turn to the interface properties. Compared to the approach of McCoy et al.,[28−30] we consider an attractive wall which leads to a wetting transition and present a quantitative comparison between the surface/interface free energies obtained from the MC simulations and the SCF calculations.

A. Surface Properties. The dependence of the monomer number density at a wall is presented in parts a and b of Figure 8. The simulations (part a) are performed in the canonical ensemble. The overall density at $\epsilon_w = 4$ is chosen such that the density far away from the wall corresponds to the density of a liquid in coexistence with the vapor. We observe three pronounced packing layers at the wall in the Monte Carlo simulations. In the SCF calculations (part b) we use the weight function (3.24) (part d) with $K = 10$ and 4 718 592 polymer conformations for the enumeration of the single chain partition function. The qualitative features of packing of the fluid against the wall are reproduced by the SCF calculations; however, the height of the first peak is severely overestimated.

It is instructive to compare the monomer density profile for $\epsilon_w = 4$ to the pressure profile in Figure 1. In the bulk, the Lennard−Jones contribution to the pressure is positive, because we are above the critical temperature of the monomer fluid. The contribution of the FENE potential to the pressure is negative, such that the total pressure nearly vanishes. The pressure profiles follow closely the monomer density. The packing peaks in the monomer density correspond to peaks in the both contributions to the pressure. In the first peak, the absolute value of the contributions perpendicular to the wall is smaller than the absolute value of lateral contribution, while this relation is reversed in the second layer.

Since we work in the canonical ensemble, the density increases in the middle of the film. We have not chosen to simulate grand canonically at the bulk value of the coexistence chemical potential, because for $\epsilon_w < 2.2$ (cf.

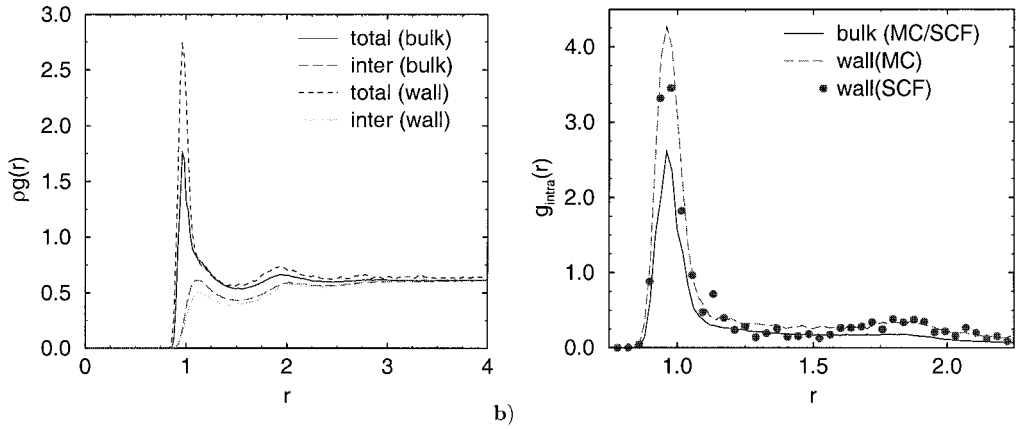

Figure 9. (a) Total and intermolecular pair correlation function $T = 1.68$ at coexistence density in the bulk $\phi = 0.611$ and in the first layer at an attractive wall ($\epsilon_w = 4, z = 1.35 \pm 0.026$ and $\phi(z) = 0.639$). In the vicinity of the wall the packing is more pronounced and the correlation hole is deeper than in the bulk. (b) Intramolecular pair correlation function $g_{intra}(r)$ in the bulk and at an attractive wall ($\epsilon_w = 4, z = 1.35 \pm 0.026$ and $\phi(z) = 0.639$ (MC) or $\phi(z) = 0.784$ (SCF)).

Figure 11) the wall is effectively repulsive and in a slitlike geometry with two repulsive walls the vapor phase is stable (capillary "drying"). Upon decreasing ϵ_w, we decrease the density in the vicinity of the wall and the strength of the packing effects; a smooth profile develops. The density rises less steeply to the coexistence value. These qualitative features are observed in the MC simulations and the SCF calculations. However, the profiles in the SCF calculations at low ϵ_w are steeper and reach the bulk value of the density sooner than the corresponding profiles in the MC simulations. Hence, the monomer−wall interaction energy is more favorable in the SCF calculations than in the MC simulations.

According to the simplistic arguments above, the density profile at a hard wall resembles an interfacial profile. For comparison, we show the interface profile in the SCF calculations in panel b. The interfacial profile has a rather extended tail at low density, but the slope at the center and the high-density portion similar to the $\epsilon_w = 1$ profile.

In parts c and d of Figure 8 we investigate the density of chain ends. To separate the packing effects on the monomer scale from the polymeric features we present the ratio between the density of chain ends and the monomer density. The chain ends are enriched at the wall, and we find a depletion a distance 2σ away from the interface. Since a chain end is connected only at one side, it has a higher entropy and explores the region at the wall more completely. Of course, a distinction between the monomeric and polymeric length scales is impossible because we have investigated only one chain length, but simulations of interfaces in blends[79,82] suggest that the length scale of the depletion is associated with the radius of gyration. Upon decreasing ϵ_w, the depletion zone moves away from the wall and becomes less pronounced. An enrichment of chain ends is also reported from neutron reflectivity experiments[83] and very similar profiles are obtained for hard chains at hard walls.[27,30]

The relative density of the polymer's center of mass is displayed in panels e and f of Figure 8. The centers of mass complement the behavior of the end monomers: they are deplete in the vicinity of the wall, but they are enriched a distance 2σ away. Again, the behavior is similar to the behavior of hard chains.[27,30] When we decrease ϵ_w, the effect becomes weaker. For both polymeric quantities we achieve quantitative agreement between the MC simulations and the SCF calculations. This shows that our partial enumeration scheme captures some details of the conformational entropy in inhomogeneous systems.

To investigate the packing in the first peak (i.e., $1.324 \le z \le 1.376$) of the density profile at the wall more closely we have monitored the pair correlation $g(\mathbf{r})$ function parallel to the wall in the first peak of $\phi(z)$ for $\epsilon_w = 4$. A comparison with the packing in the bulk is shown in Figure 9a. We first note that both peaks in the total pair correlation function are more pronounced at the wall than in the bulk. This suggests that the layering perpendicular to the wall also increases the structure parallel to it. Similar changes in the pair correlation function are also observed in simple liquids.[84] The intermolecular pair correlation function $g_{inter}(\mathbf{r})$, which is associated with the distance of monomers of different chains, shows a deeper correlation hole at the wall than in the bulk. This indicates that the conformations of the polymers, as they pack against the wall, are more two-dimensional and therefore there is less interpenetration among different chains. Changes of the intermolecular (lateral) packing as the wall is approached are, however, not captured by our SCF calculations. This might be one reason for the slightly different packing effects of the MC simulations and the SCF calculations in the vicinity of the wall.

Some of the changes in the intramolecular packing $g_{intra}(\mathbf{r}) = g(\mathbf{r}) - g_{inter}(\mathbf{r})$ are associated with a modifications of the single chain conformations by the wall. These effects are partially captured in our SCF scheme. Since we use the chain conformations of the liquid in the SCF calculations the intramolecular pair correlation function in the MC simulations and the SCF calculations is identical by construction. Figure 9b presents the results for the intramolecular pair correlation function between monomers of the same chain in the first peak of the density profile at the wall as a function. The first peak of g_{intra} at $r \approx 0.96$ is enhanced by almost a factor 2 compared to the bulk behavior. The SCF calculations are able to reproduce such a change in the intramolecular packing parallel to the wall. This finding can be rationalized via the geometric restriction posed by the wall. If one monomer of a chain is located close to the wall its neighbors along the polymer will also have a high probability to be found in the first peak of the monomer density profile, because they can explore only

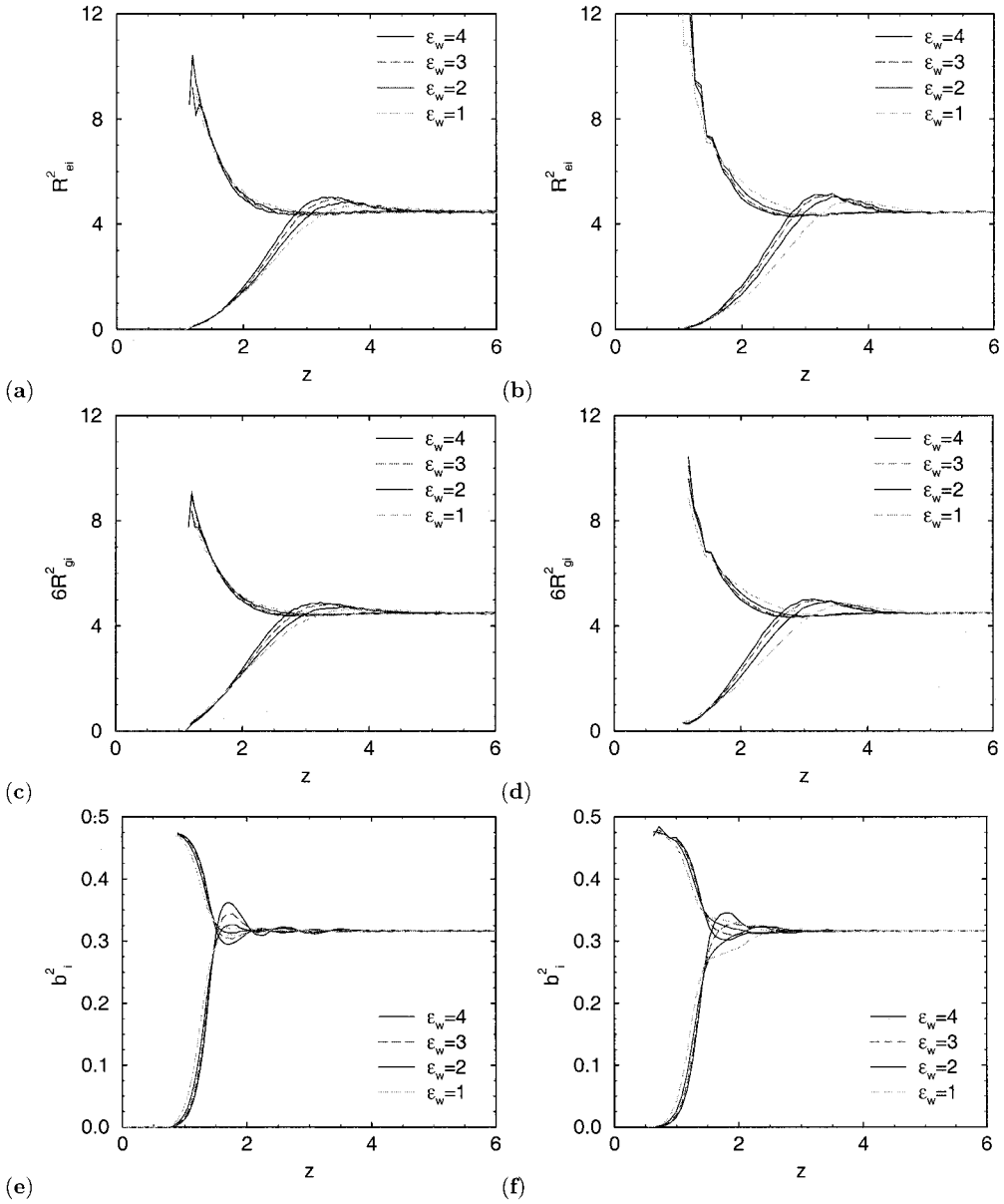

Figure 10. Orientational profiles as a function of the monomer−wall interaction ϵ_w. The left column (a, c, e) corresponds to the Monte Carlo simulations; the right column (b, d, f) shows the results of the SCF calculation with $K = 10$. Parts a and b present the parallel and perpendicular component of the end-to-end distance as a function of the distance between the center of mass and the wall for $\epsilon_w = 4$, 3, 2, and 1 from above to below. Panels c and d display the results of the radius of gyration, while panels e and f show results for the vector between bonded neighbors along the chain.

a half sphere with $z \gtrsim 1$ around the monomer rather than a complete sphere as in the bulk.

The detailed conformations of the polymers at the wall are studied in Figure 10. The lateral and perpendicular components of the end-to-end vector in the MC simulations and the SCF calculations are shown in parts a and b, respectively. The distance between the center of mass and the wall is used as a z coordinate of these polymeric properties. As expected the lateral components increase at the surface, while the perpendicular extension of the chains decreases upon approaching the wall. This finding is compatible with the increase of the correlation hole (in the parallel direction) close to the wall. Note that at a distance $z \approx 3.5\sigma$, the behavior is inverted: the lateral extension have reached their bulk value while the perpendicular extension is actually slightly larger than in the bulk. Such an overshoot has also been observed in the bond fluctuation model and can be reproduced by SCF calculation in the framework of the Gaussian chain model.[38] Upon decreasing the attractive strength of the wall, the effect decreases. The radius of gyration shows a behavior very similar to the behavior of the end-to-end vector. Its orientation in the MC simulations and the SCF calculations is displayed in panels c and d, respectively. Note that the relation $R_e^2 = 6R_g^2$, which holds for Gaussian chains, is fulfilled in the middle of the film even for our very short chains. The behavior of bonding vectors between neighbors along the chain is investigated in parts e and f. The z coordinate corresponds to the midpoint of the bond. First, we note that the range over which the orientation of bonds extends is smaller than the orientation of the chain properties. Only the bonds in the ultimate vicinity of the walls are aligned parallel to the surface. A similar behavior has been observed in density functional calculations of Kierlik and Rosinberg[27] for hard chains and

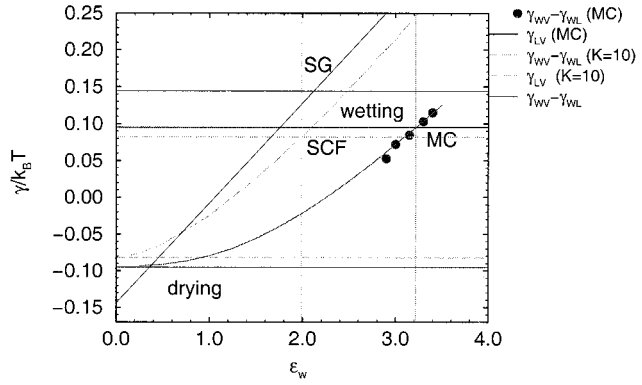

Figure 11. Dependence of the surface free energy difference $\gamma_{WV} - \gamma_{WL}$ on the attractive strength of the wall. Circles denote the measurement via the reweighting technique, while the solid curve presents the result of the simulations in the expanded ensemble. The curve is shifted vertically as to match the results of the reweighting technique. The horizontal (thick) solid lines mark the value of the interfacial tension γ_{LV}, the vertical lines mark the location of the wetting transition. Dashed lines correspond to the SCF calculations. Thin solid lines mark the behavior in the square gradient approximation.

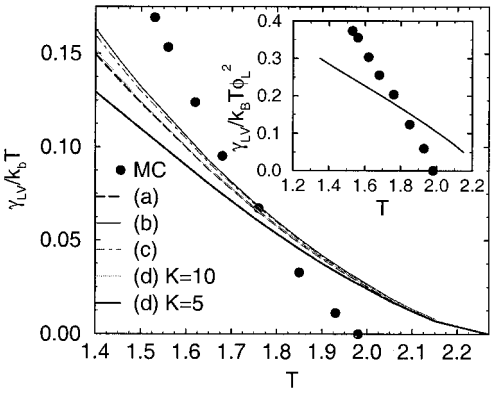

Figure 12. Temperature dependence of the interfacial tension γ_{LV}. The symbols correspond to the MC results, while the lines correspond to the SCF theory with different weighting functions (according to eq 3.24, parts a, b, etc.). The inset shows the ratio $\gamma_{LV}/\phi_{coex}^{L2}$, which is expected to reach a plateau value for low temperatures/long chain lengths in the square gradient approximation.

in MC simulations of other models.[60,85,86] The MC simulations show that at a distance 1.75σ away from the wall this orientation is inverted; i.e., bonds are aligned perpendicular to the wall. This effect is more pronounced in the MC simulations than in the SCF calculations. For distances larger than 2σ, the orientation is isotropic. The inversion of the bond orientation becomes weaker as we decrease ϵ_w. The agreement between the SCF calculations and the MC simulations for the orientation and deformation of the polymer coil in the vicinity of the surface and its dependence on the monomer−wall interaction is quantitative, and even on the very short length scales of the distance between neighboring monomers the SCF calculations give a faithful account. This indicates again an accurate treatment of the conformational degrees of freedom in the SCF calculations.

Now we turn to the dependence of the surface free energy on ϵ_w. Our results are summarized in Figure 11. For a few values in the range $2.9 \leq \epsilon_w \leq 3.4$, we have determined the free energy difference between the vapor and the liquid in contact with the wall directly in the MC simulations. These values are shown by filled circles. For other values of the attractive strength ϵ_w we used thermodynamic integration. The result is displayed as solid curve. The free energy of the wall results from a balance between two effects: On one hand, the liquid lowers its energy because of the attractive forces between the walls and the monomers. On the other hand, the polymers loose conformational entropy at the wall. For $\epsilon_w > 2.26$ the attractive forces dominate and the wall favors the fluid, while it attracts the vapor for smaller values of ϵ_w. For values $\epsilon_w < \epsilon_w^{dry} \approx 0.5$, it was not possible to determine γ_{WL}, because the vapor appears to dry the wall; i.e., our grand canonical simulations at the coexistence value of the chemical potential eventually end up in the vapor phase. Indeed, the difference of the surface free energies equals in magnitude the interfacial tension. The latter quantity is shown as a horizontal line (cf. section IVc).

The SCF calculations are shown as a dashed curve. They reproduce the qualitative features of the MC results, namely, a rather weak increase of $\gamma_{WV} - \gamma_{WL}$ for small ϵ_w and a more steep increase at a larger attractive strength. However, the actual value of the surface free energy difference is overestimated by the SCF calculations. The SCF calculations yield a too large value at $\epsilon_w = 0$ and predict a too rapid increase of $\gamma_{WV} - \Gamma_{WL}$ with ϵ_w at small values of the attractive strength. The slope of curve is, however, in fair agreement with the MC data at larger values of ϵ_w.

The major contribution to the free energy difference stems from the liquid, and the slope of the curve is determined by the energy contribution of the monomer−wall interaction (cf. eq 2.8), which, in turn, is a functional of the density profile close to the wall. As shown in parts a and b of Figure 8, the density rises faster in the SCF calculations than in the MC simulations (for $\epsilon_w = 1$). Therefore, the energy contribution of the monomer−wall interaction is more negative in the SCF calculations, and hence, the surface free energy difference rises faster with ϵ_w in the SCF calculations than in the MC simulations. This observation suggests that the deviation between the MC simulations and the SCF calculations arise due to an inappropriate description of the low-density tail in the density profile of a liquid close to a (repulsive) wall.

B. Interface Properties. We have measured the interfacial tension γ_{LV} between the coexisting liquid and vapor phase via the reweighting technique in the grand canonical simulations. The temperature dependence of γ_{LV} is presented in Figure 12. Symbols refer to the MC data, while the lines display the SCF results. Different lines correspond to different choices of the weight function according to eq 3.24. The interfacial tension vanishes at the critical point. At high temperatures, the interfacial tension is overestimated by the SCF theory. This is expected, because the SCF theory also overestimates the critical temperature and the interfacial tension vanishes with an exponent $^3/_2$ in the mean field calculations while it decreases with an exponent $2\nu \approx 1.24$ upon approaching T_c in the simulations. Surprisingly, the SCF calculations underestimate the interfacial free energy at low temperatures. This behavior appears to be largely independent of the weight function and we believe that is is not associated with the local packing. We rather speculate that this underestimation is due to the failure of the TPT1 approximation (upon which the SCF calculations are based) to describe the

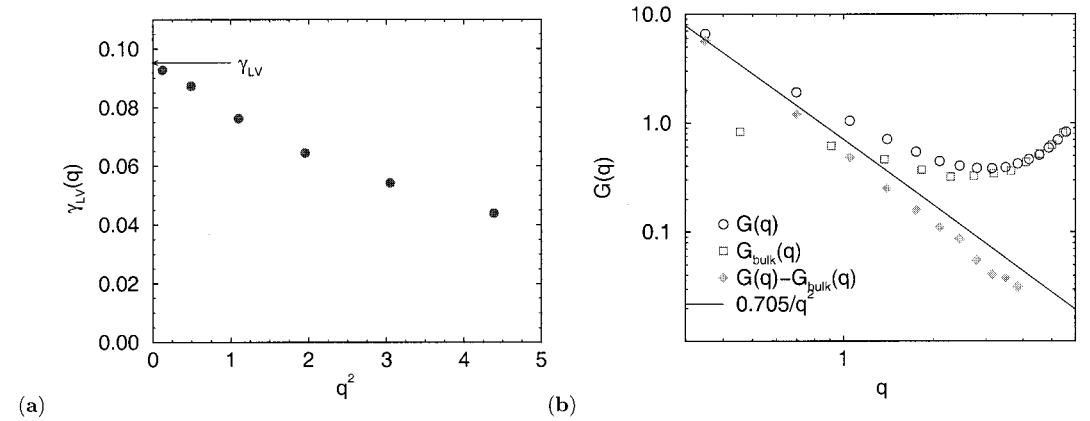

Figure 13. (a) Fluctuation spectrum of the local interface position. The arrow marks the value of the interfacial tension obtained from the reweighting method. (b) Global scattering intensity from a system containing two interfaces and the bulk system. The straight line corresponds to capillary waves with the value of the interfacial tension $\gamma_{LV} = 0.0953$ as measured independently in the simulations.

(hypothetical) structure of a homogeneous low density polymer solution appropriately. To calculate the phase boundaries, we need only the free energy close to the coexistence densities. The vapor phase at low temperatures is nearly ideal, and the ideal gas contribution is captured correctly by the TPT1 theory. Hence, we obtain rather good agreement for the binodals at low temperatures. The calculations of the interface and surface free energies involve, however, the free energies for all compositions inside the miscibility gap. Hence, these quantities provide a sensitive test how the free energy density is extrapolated inside the two phase region. Clearly, the structure of a polymer solution and a Lennard−Jones monomer fluid differs appreciably at low density and the TPT1 approximation fails. This holds *a fortiori* close to the critical point of the Lennard−Jones monomer fluid, which is inside the miscibility gap. The associated singularities of the free energy of the reference systems are not removed by first-order perturbation theory. For a better quantitative description of the excess free energies in inhomogeneous polymer solutions our approach requires an improved description of the free energy inside the miscibility gap.

The simple square gradient approximation and scaling considerations suggest that the interfacial tension increases such as the square of the liquid density at low temperatures. The inset of Figure 12 shows this ratio. For the temperatures available neither the MC simulations nor the SCF calculations show a plateau in $\gamma_{LV}/\phi_{coex}^{L2}$. This is perhaps not too surprising, because the interfacial tension increases with the chain length for the incompatibility and chain length investigated, and only substantially longer chains might exhibit the simple scaling behavior.

To investigate the local structure at the interface in more detail, we performed simulations in the canonical ensemble at $T = 1.68$ and a $18 \times 18 \times 36$ geometry with periodic boundary conditions in all directions. Two liquid−vapor interfaces form a distance $18 \approx 11R_g$ apart. A quantitative comparison between MC simulations and SCF profiles has to take due account of interfacial fluctuations. While the SCF profiles correspond to a perfectly flat interface, the local position of the interface is fluctuating in the MC simulations.[79,82,94] These fluctuations increase the interface area and for large wavelength they are describable by the capillary wave Hamiltonian.[87] Let $u(x,y)$ be the local interface position; then the Hamiltonian for the deviations of the local position u is given by

$$H = \int \mathrm{d}x\mathrm{d}y \, \frac{\gamma_{LV}}{2} (\nabla_{||} u)^2 \tag{4.1}$$

In our simulations, we define a local y averaged interfacial position $u(x)$ by minimizing[88,79]

$$\left| \int_{x-0.25}^{x+0.25} \mathrm{d}x' \int_0^D \mathrm{d}y' \int_{u(x)-3.6}^{u(x)+3.6} \mathrm{d}z' \left(\phi(x',y',z') - \frac{\phi_{coex}^{L}}{2} \right) \right| \tag{4.2}$$

This coarse-grained quantity describes the shape fluctuations of the interface and is rather insensitive to local bulklike density fluctuations. The interface position is Fourier decomposed according to

$$u(x) \sim \frac{a_0}{2} + \sum_k [a(q_k) \cos(q_k x) + b(q_k) \sin(q_k x)] \tag{4.3}$$

with wave vectors $q_k = 2\pi k/L$. With this coarse-grained $u(x)$ in the capillary wave Hamiltonian, the equipartition theorem yields for the Fourier components $a(q)$ and $b(q)$

$$\gamma_{LV}(q) = \frac{2k_B T}{L^2 q^2 \langle a^2(q) \rangle} = \frac{2k_B T}{L^2 q^2 \langle b^2(q) \rangle} \tag{4.4}$$

In principle, the so-determined value of the interfacial tension also depends on the wavevector q, and we obtain the macroscopic interfacial tension $\gamma_{LV} = \gamma_{LV}(q \to 0)$ in the limit of small wavevectors. The results of the MC simulations are presented in Figure 13a. Indeed, the MC data agree with the value of the interfacial tension determined with the reweighting method in the limit $q \to 0$. However, we find a pronounced reduction of the effective interfacial tension at larger q vectors. Similar deviations have recently been predicted by Mecke and Dietrich[89] in density functional calculations for a Lennard−Jones monomer fluid.

The capillary waves are also detectable in the total scattering function for wavevectors $\mathbf{q}$ parallel to the interface.[90−92] For a system with two independent interfaces the increase of the scattering due to capillary waves takes the form $\Delta G(\mathbf{q}_{||}) \approx (2\Delta\phi^2 L^2/nN)\,(k_B T/\gamma_{LV} q^2)$.

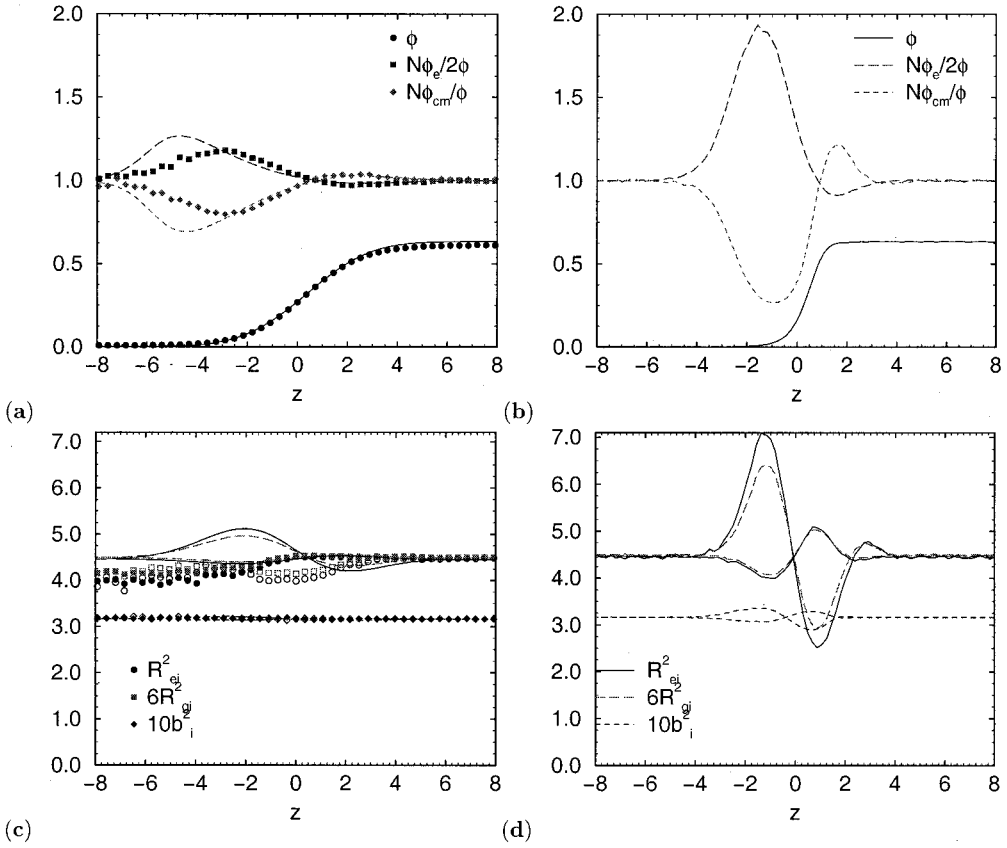

Figure 14. Interface profiles at $T = 1.68$. Key: (a) monomer density and relative densities of chain ends and center of mass locations. Symbols present laterally averaged MC results ($L = 18$), while lines refer to SCF results convoluted with a Gaussian of width $s = 1.9$. (b) The "intrinsic" profiles in the SCF calculations. (c) Orientations of the end-to-end vector, the radius of gyration and the vectors between bonded neighbors. The symbols display the laterally averaged MC results. Filled symbols correspond to the components parallel to the interface, while open symbols refer to the perpendicular component. The lines denote SCF results which are convoluted with a Gaussian of width $s = 1.9$. (d) The corresponding "intrinsic" profiles in the SCF calculations.

$\Delta\phi = \phi_{\text{coex}}^{\text{L}} - \phi_{\text{coex}}^{\text{V}}$ is the density difference of the liquid and the vapor. The MC results for the scattering of a system with two interfaces are presented in Figure 13b. The total scattering of the bulk is also shown. For small wavevectors the MC data are well describable by the expression above; for finite wavevectors, however, there are deviations. We do not expect that interactions among the two interfaces in our system are the major source for the deviations, because these interactions would also modify the fluctuations for small wavevectors.

The density profiles across the liquid−vapor interface are presented in Figure 14. The symbols in panel a correspond to the profiles in the MC simulations, which are laterally averaged over the whole system size $L = 18$. Clearly, they are much broader than the corresponding profiles in the SCF calculations (panel b).[93] The capillary wave Hamiltonian shows that the local interface positions are Gaussian distributed according to

$$P_{\text{L}}(u) = \frac{1}{\sqrt{2\pi s^2}} \exp\left(-\frac{u^2}{2s^2}\right) \text{ with}$$

$$s^2 = \frac{1}{4\pi^2}\int \mathrm{d}^2 q \frac{k_{\text{B}}T}{\gamma_{\text{LV}}(q)q^2} \approx \frac{1}{2\pi\gamma_{\text{LV}}} \ln\frac{L}{B_0} \quad (4.5)$$

where B_0 is an unknown small distance cutoff below which a description via the capillary Hamiltonian breaks down. The effect of capillary waves on the laterally averaged profiles $p_Q(z)$ of a quantity Q can be accounted for by a convolution of the "intrinsic" profile $p_{Q\text{int}}$ associated with an ideally flat interface and the distribution of the local interface positions:[74,82,94]

$$p_Q(z) = \int \mathrm{d}z'\, p_{Q\text{int}}(z') P_{\text{L}}(z - z')$$

(convolution approximation) (4.6)

The results of convoluting the SCF profiles with a Gaussian are displayed in panel a as lines. The width of the Gaussian $s = 1.9$ is chosen as to achieve good agreement between the MC data and the convoluted SCF profiles for the monomer density. For all other profiles we employ the same value of s. Note, however, that the coexistence density of the liquid is larger in the SCF calculations than in the MC simulations, and it is not obvious that the SCF calculations yield an accurate description of the intrinsic interface profile. Hence, deficiencies of the SCF calculations might be attributed to capillary waves and might affect the value of s.

Upon approaching the interface from the liquid side (right) the center of mass density increases and the relative density of chain ends is reduced, respectively. The broadened SCF profiles capture the strength of the effect as well as its spatial extension. At the center of the interface the behavior changes: the relative density of chain ends is increased and the center of mass density is reduced; i.e., the polymers stick out their ends into the vapor phase. The behavior on the liquid side

resembles much its analogon at a wall and the SCF calculations yield again a quantitative description. The agreement on the vapor side is less satisfactory: The SCF calculations overestimate the enrichment of chain ends and the reduction of the center-of-mass density; they also overestimate the distance at which a uniform distribution is reached. The SCF profiles in the vapor close to the interface are dominated by polymer configurations which are strongly elongated in the *z* direction so as to reach the liquid phase. In the Monte Carlo simulations, however, the chains in the vapor phase do not decrease their energy by reaching out to the liquid and increasing the number of favorable intermolecular interactions, but they shrink into a globule and thereby increase the number of intramolecular interactions. This mechanism is not captured by the present SCF scheme.

The profiles of the parallel and perpendicular components of the chain extensions are compared in parts c and d of Figure 14. The SCF profiles (part d) exhibit a significant increase of the perpendicular chain extension on the vapor side. This indicates again that the chains in the SCF scheme stretch so as to reach the liquid. The comparison of the convoluted profiles and the MC simulations shows that the SCF calculations overestimate the effect. The MC simulations reveal instead that the chains are slightly shrunken in the vapor phase. On the liquid side, the chains align parallel to the interface as they do at a wall. The effect is more pronounced in the simulations than in the SCF calculations. There is hardly any orientational effect detectable in the convoluted profiles of the bond orientation. The SCF profiles suggest that the bond vectors align parallel to the interface on the liquid side and perpendicular on the vapor side, but the effect is much smaller than for the overall chain extension. A very similar behavior is observed at interfaces in binary polymer melts.[82]

Interestingly, the liquid side of the SCF profiles resemble strongly the corresponding part of a profile at a wall with small attractive strength. The presence of the wall strongly reduce fluctuation effects, but the shape of the "intrinsic" interface profile and a surface profile (close to the drying transition) are very similar.

C. Wetting Behavior. Upon increasing the attractive strength ϵ_w of the wall, the surface free energy of the liquid decreases and we encounter a wetting transition.[95,96] Upon approaching the coexistence line $\mu \to \mu_{coex}^-$ the adsorbed amount stays finite for $\epsilon_w < \epsilon_w^{wet}$ (partial wetting), while it diverges for larger attractive strengths (complete wetting). In the latter case, there is a layer of thickness l at the wall and the surface contribution to the thermodynamical potential $G(\epsilon_w, \mu)$ can be approximated by

$$\frac{L^2}{G_s} \approx \gamma_{WL} + \gamma_{LV} + \Delta\phi\epsilon_w\left(\frac{9}{l^8} - \frac{3f_w}{l^2}\right) + \Delta\mu\frac{\Delta\phi}{N}l \qquad (4.7)$$

where $\Delta\mu = \mu - \mu_{coex}$ denotes the distance from the liquid−vapor coexistence curve. The equilibrium thickness of the wetting layer is determined by the condition $\partial G_s/\partial\mu = 0$, which yields[95]

$$l^3 \approx \frac{6f_w\epsilon_w N}{\Delta\mu} \text{ (complete wetting)} \qquad (4.8)$$

To locate the position of the wetting transition roughly, one can start with the vapor in contact with the wall at small ϵ_w. In the grand canonical simulations at the coexistence value of the chemical potential, the surface is only partially wet and there is only a very small enrichment of polymers at the wall. Upon increasing the attractive strength of the wall, the absorbed amount increases. At the wetting transition, there is a macroscopic thick layer at the wall, i.e., the adsorbed amount Σ diverges. The results for such a simulation suite are presented in Figure 15 for the temperature $T = 1.68$. The results were averaged over 32 independent runs. Starting at $\epsilon_w = 2 < \epsilon_w^{wet}$ we increased slowly the attractive strength of the wall. The systems were equilibrated 100 000 configurational bias tries before data were collected, the adsorbed amount and its fluctuations were averaged over another 100 000 insertion/deletion attempts, and then we incremented ϵ_w. At around $\epsilon_w = 3.4$, the adsorbed amount and its fluctuations increase strongly. This is an indication of the vicinity of the wetting transition. Though the simulations are useful for a rough location of the transition, neither the order of the wetting transition nor the accurate value of ϵ_w at the transition can be infered from the data.

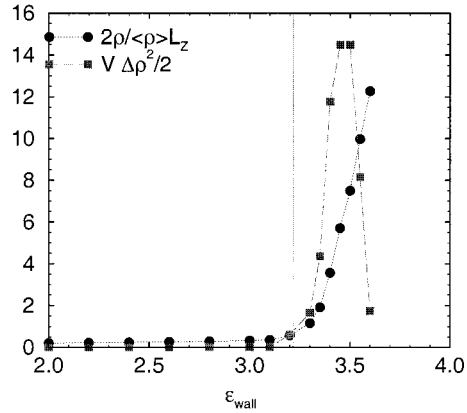

Figure 15. Determination of the wetting transition temperature via the temperature dependence of the layer thickness upon increasing the temperature. Circles correspond to the layer thickness, while squares refer to the fluctuations of the layer thickness. The lateral system size is $L = 13.8$. The transition temperature of the first order wetting transition (indicated by the vertical line) is severely overestimated.

Having determined the interfacial tensions and the difference in the surface tension, we can locate the wetting transition temperature via the Young equation.[60] According to the Young equation, the liquid wets the surface if the difference in the surface free energies of the vapor and the liquid exceeds the interfacial tension:

$$\gamma_{WV} - \gamma_{WL} > \gamma_{LV} \Rightarrow \text{liquid wets the wall} \qquad (4.9)$$

This behavior is investigated in Figure 11. The solid curves mark the difference in surface free energies while the horizontal line marks the value of the interfacial tension. The wetting transition occurs at $\epsilon_w^{wet} = 3.22$. Since the two free energy curves intersect at a finite angle, the wetting transition is of first order. Therefore, the absorbed amount jumps at the wetting transition from a small finite value to a macroscopic one. The associated free energy barrier between the two states also explains the gross overestimation of the attractive strength required to bring about the wetting in the simulation suite discussed above. The finding is also consistent with simulation studies of monomeric Len-

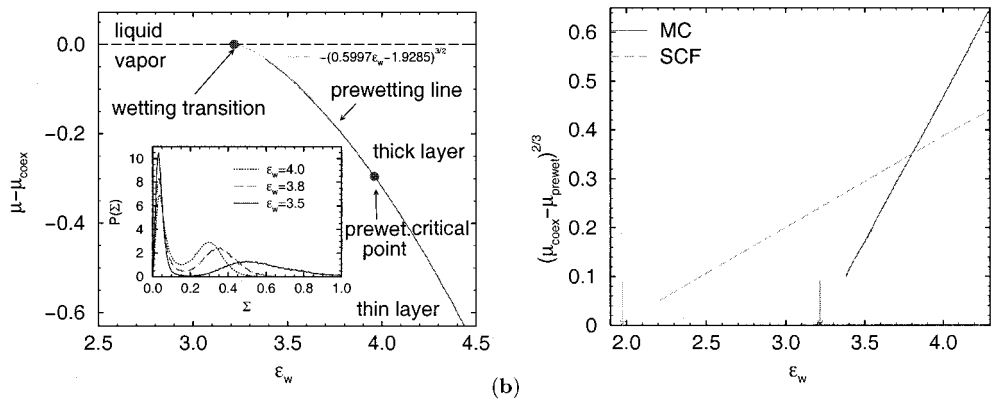

Figure 16. (a) Wetting and prewetting at $T = 1.68$. The horizontal dashed line marks the liquid vapor coexistence, the solid curve presents the results for the prewetting line (and its finite size extension). In the vicinity a fit according to the Clapeyron equation (eq 4.12) is shown. The wetting transition and the prewetting critical point are marked. The inset shows the probability distribution of the layer thickness on the prewetting line for a small system $L = 13.8$. (b) Locating the first-order wetting transition by extrapolating the prewetting line to the phase coexistence. The solid line corresponds to the MC results obtained via (single) histogram extrapolation, while the dashed line corresponds to the SCF result. The extrapolated values of the wetting transition are indicated by arrows.

nard−Jones fluids,[61,97] which also find a strong first-order wetting transition.

The SCF calculations, shown as a dashed line, yield a qualitatively similar behavior, but the value $\epsilon_w^{wet} = 1.99$ at the first-order wetting transition is much smaller than in the MC simulations. The simple square gradient calculations yield a value $\epsilon_w^{wet} = 2.43$. However, the better agreement of the latter with the MC simulations is completely fortuitous. The square gradient considerations yield for the interfacial tension and the difference in the surface free energy worse values than the SCF calculations.

As already noted, the difference of the surface free energies approaches $-\gamma_{LV}$ for small values of ϵ_w and the vapor drys the wall. In the SCF calculations and the MC simulations the free energy difference approaches the value $-\gamma_{LV}$ with a very small slope. This indicates that the transition is very weak first order, and we cannot rule out a second-order transition. In the SCF calculations the drying occurs very close to $\epsilon_w \approx 0$. In the MC simulations it was not possible to investigate values $\epsilon_w < 0.5$ (cf. section IVa). The weakness of the transition explains the lack of metastability which is observed in the simulations. A very similar behavior is found for monomeric Lennard−Jones fluids,[61,97] and a careful study of finite size effects is necessary[97] to accurately pinpoint the location of the drying transition and its order. This is not attempted in the present study.

Since the wetting transition at $\epsilon_w = 3.22$ is first order, there is a concomitant jump in the layer thickness above the wetting temperature away from the coexistence curve in the $\epsilon_w - \mu$ plane, i.e., at $\mu < \mu_{coex}$. At this prewetting line, a thin absorbed layer coexists with a thick layer. In the inset of Figure 16 we show the probability distribution of the areal polymer number density $\Sigma = n_l/L^2$ at a single wall for attractive strengths slightly above the wetting transition. n_l denotes the number of polymers with center of mass position $z_{cm} < D/2$. The data were obtained for the lateral system size $L = 13.8$. One clearly observes a bimodal distribution which indicates the coexistence of two layers with different thickness. The chemical potential is adjusted as to give equal weight to both peaks. The corresponding prewetting line in the $\epsilon_w - \mu$ plane is presented in Figure 16. Increasing the attractive strength ϵ_w of the surface (or the temperature) we decrease the difference in the thickness of the coexisting layers and the chemical potential at which the two layers of different thickness coexists moves further away from value of the liquid−vapor coexistence.

The approach of the prewetting to the coexistence curve has been studied by Hauge and Schick.[98] The differential of the surface contribution to the thermodynamic potential $G(\epsilon_w, \mu)$ is given by (cf. eq 2.8)

$$\frac{dG_s}{L^2} = \frac{\langle E_{wall}\rangle}{\epsilon_w L^2} d\epsilon_w - \Sigma^{ex} d\Delta\mu \qquad (4.10)$$

$\Sigma^{ex} \approx \Delta\phi l/N$ denotes the polymer excess in the enrichment layer of thickness l at the surface. At the prewetting line, a thin l_{thin} and a thick layer l_{thick} coexist, and hence, their change in G_s along the prewetting line is the same. This yields the following Clapeyron equation:[98]

$$\frac{d\Delta\mu}{d\epsilon_w}\Big|_{prewet} = \frac{(\langle E_{wall}\rangle_{thick} - \langle E_{wall}\rangle_{thin})/\epsilon_w L^2}{\Sigma^{ex}_{thick} - \Sigma^{ex}_{thin}} \qquad (4.11)$$

Close to the coexistence curve, l_{thick} is very large. The difference in the surface excess increases to leading order linear $\Sigma^{ex}_{thick} - \Sigma^{ex}_{thin} \approx \Delta\phi l_{thick}/N$ while the difference in the wall energies approaches a constant value with growing l_{thick}. To a rough approximation this constant takes the value $-\Delta\phi(9/l_{thin}^8 - 3f_w/l_{thin}^2)$.

$$\frac{d\Delta\mu}{d\epsilon_w}\Big|_{prewet} \approx -\frac{N(9/l_{thin}^{\ 8} - 3f_w/l_{thin}^{\ 2})}{l_{thick}} \sim \Delta\mu^{1/3} \qquad (4.12)$$

According to eq 4.8 the layer thickness increases as $l_{thick} \sim |\Delta\mu|^{-1/3}$ above the wetting transition temperature (complete wetting). Integration of eq 4.12 yields $\Delta\mu|_{prewet} \sim (\epsilon_w - \epsilon_w^{wet})^{3/2}$.[98] This dependence can be used to extrapolate the prewetting line toward the coexistence curve and estimate the location of the wetting transition. The approach of the prewetting line in the MC simulations and the SCF calculations is presented in Figure 16b. The extrapolation yields the accurate estimate $\epsilon_w^{wet} = 3.22$ for the MC simulations and $\epsilon_w^{wet} = 1.98$

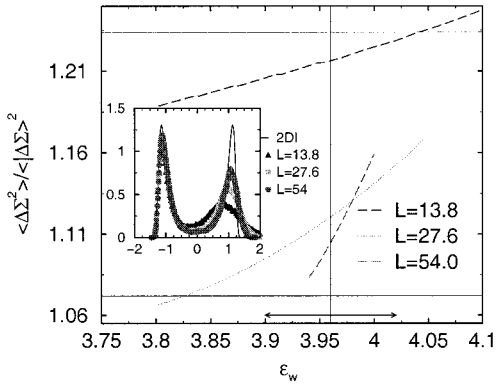

Figure 17. Locating the prewetting critical point using the cumulant intersection method. The lower horizontal line corresponds to the 2D Ising value of the cumulant, the upper horizontal line marks 3D Ising critical behavior. The inset displays the probability distribution of the layer thickness normalized to zero mean and unit variance for the system size L = 13.8, 27.6, and 54 at T = 1.68 and ϵ_w = 3.96. At the transition the normalized distribution depends only on the universality class and the corresponding function for the 2D Ising model is also shown.

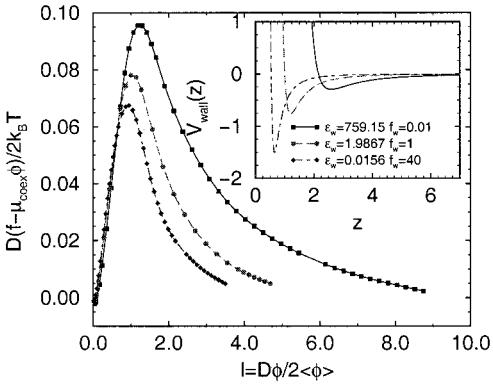

Figure 18. Influence of the shape of the wall potential on the order of the wetting transition. $V_{wall}(z) = \epsilon_w(1/z^9 - f_w 1/z^3)$. The integrated wall energy scales as $\epsilon_w f_w^{4/3}$.

for the SCF calculations. The rather strong deviations for the slope between the MC simulations and the SCF calculations can be traced back to the strong dependence on the energy of the thin layer l_{thin} in eq 4.12. Since the wetting transition is strongly first order, the adsorbed film is very thin and might not be homogeneous in the lateral direction but rather consists of isolated adsorbed chains at the wall in the MC simulations. This situation is, however, not described in the SCF calculations, which assume lateral homogeneity from the very beginning.

The prewetting line ends in the prewetting critical point. Here, the difference in the layer thicknesses vanishes. This transition is believed to belong to the 2D Ising universality class. Since the correlation length of density fluctuations parallel to the surface diverges at this point, effects of the finite lateral extension of the simulations cell have to be investigated carefully. An attempt to locate the prewetting critical point via a finite size scaling analysis is shown in Figure 17. We plotted the cumulant ratio $(\langle\Sigma^2\rangle - \langle\Sigma\rangle^2)/\langle|\Sigma - \langle\Sigma\rangle|\rangle^2$ along the prewetting line for several values of the lateral systems size. At the prewetting critical point, cumulants of different system sizes are expected to intersect in a common point.[99] The cumulant value at this intersection point is universal. The values of the 3D Ising and 2D Ising universality are indicated by the higher and lower horizontal lines, respectively. For the pair of system sizes L = 13.8 and 27.6, no intersection point is found close to the universal value. The value of the cumulant at the intersection is even larger as the value of the 3D Ising universality class. For L = 27.6 and 54, we obtain an intersection around ϵ_w = 3.98, and the cumulant value at the intersection is between the 3D and 2D Ising universality class. Assuming that the intersection point approaches the 2D Ising value we estimate the location of the prewetting critical point to be between the intersection for our two largest systems and the value for which the cumulant of the largest system size attains the 2D Ising value ϵ_w = 3.93. Thus, our estimate for the prewetting critical point is ϵ_w^{pwc} = 3.96(6). The sign of the shift of the cumulant intersection point is the same as in the 3D Lennard Jones monomer fluid.[100] The normalized probability distribution of the layer thickness at our estimate for the prewetting critical point is presented in the inset of Figure 17. Because of field mixing effects[100] the distribution is asymmetric, but upon increasing the system size we decrease the asymmetry of the distribution and the simulation data approach the universal curve of the 2D Ising universality class. The value ϵ_w^{pwc} = 3.96 is also marked in the phase diagram (Figure 16). Snapshots reveal that even the system size L = 54 is by far not large enough to exhibit the self-similar structure of the 2D Ising critical point and rather pronounced correction to the leading finite size scaling effects have to be anticipated. Unfortunately, the equilibration of larger systems is beyond our computational facilities.

The prewetting line in the SCF calculations extends to larger values of the attractive strength ϵ_w. On one hand, this is expected, because the strong 2D Ising-like fluctuations are not captured in the SCF calculations. Hence the SCF calculations tend to overestimate the prewetting critical point. A similar behavior is also observed in binary polymer blends.[60] On the other hand, for strong attraction between the liquid and the wall, the density at the wall becomes very high $\phi > 1$ and our equation of state is inaccurate for such high densities.

Though we achieve only qualitative agreement between the MC simulations and the SCF calculations for the wetting properties, the latter are useful due to their computational efficiency. The SCF calculations require roughly 2−3 orders of magnitude less computational effort than the MC simulations, and this allows us to explore the influence of various parameters (e.g., chain length, temperature). We illustrate this by investigating the role of the shape of the monomer−wall interaction on the location and the order of the wetting transition at T = 1.68. We have varied the parameter f_w in the monomer wall potential (eq 2.3) and located the wetting transition. Since the attractive energy between the wall and the fluid scales approximately like $\epsilon_w f_w^{4/3}$, ϵ_w^{wet} increases with decreasing f_w. Wetting transitions occur at (ϵ_w = 759.15, f_w = 0.01), (ϵ_w = 1.987, f_w = 1), and ϵ_w = 0.0156, f_w = 40). The shape of the monomer wall potential at the wetting transition is presented in the inset of Figure 18. Increasing f_w the potential develops a deep and narrow attractive region. The free energy as a function of the density or the thickness of the absorbed layer, respectively, is shown in the main panel. The pronounced maximum around $D\phi/2\phi_{coex}^{L} \approx 1$ separates the two coexisting states: a layer of nearly

vanishing thickness and a macroscopically thick layer. Upon increasing f_w, the height of the barrier between these two coexisting states decreases, but for plausible values of f_w the barrier remains and the wetting transition is of first order.

V. Summary and Discussion

We have studied interfaces and surfaces of polymer solutions in the framework of a coarse-grained off-lattice model. The detailed conformations of the polymers and the density profiles at surfaces and interfaces, and the concomitant excess free energies have been obtained from Monte Carlo simulations and self-consistent field calculations. The self-consistent field scheme is similar to the density functional theory by Yethiraj and Woodward[34] and McCoy and collaborators.[28] The thermodynamic properties of the homogeneous state were calculated using thermodynamic perturbation theory (TPT1) with respect to the bonding potential. These calculations involve no adjustable parameter. For a spatially homogeneous system our SCF scheme reproduces the thermodynamic properties of the TPT1 and the conformational properties of the liquid phase by construction. The SCF calculations for the inhomogeneous system invoke a weighted-density functional ansatz for the monomer−monomer interaction. The weight function w parametrizes the local structure of the fluid and can be related to its direct correlation function. In the present comparison between MC simulations and SCF calculations, however, we treat w as an adjustable function and the consequences of different shapes w have been explored. The detailed form of the function does influence details of the density profiles at a wall, but the free energy values appear to be rather insensitive to our choice, just as the free energy of the homogeneous system is independent from w.

The SCF calculations are in good qualitative agreement with the MC results. For the dependence of the chain conformations at a surface (orientations of chains and bonds, enrichment of chain ends) even quantitative agreement is achieved. These quantities are determined by the modification of the weight of the different chain conformers at the surface. Using the detailed chain architecture of the computational model, we capture the effects of conformational entropy in the SCF calculations. The packing structure of monomers at the surface is, however, only qualitatively predicted by the SCF calculations. For physically plausible choices of the weight function w, we reproduce the salient features of the packing, but the first peak in the monomer density at the surface is overestimated. Additionally, our Monte Carlo simulations show that the packing of the monomers parallel to the wall depends slightly on the distance from the wall. This effect is also known from simple liquids,[84] and our one-dimensional parametrization of all spatial dependencies in the SCF calculations cannot capture these effects.

Profiles of segment densities and orientations on different length scales across the liquid−vapor interface have been investigated. Taking due account of capillary waves at the interface, the MC results and SCF calculations agree qualitatively. The agreement is almost quantitative on the liquid side of the interface, while we observe more pronounced deviations on the vapor side of the profiles.

The excess free energies of surfaces and interfaces are only qualitatively predicted by the SCF theory. At high temperatures, the interface free energy between the liquid and the vapor is overestimated by the SCF theory. Invoking a mean field approximation, our SCF calculations neglect density fluctuations. Therefore, the SCF calculations overestimates the critical temperature and yields parabolic binodals close to the critical point. At low temperatures, however, the SCF calculations underestimate the interfacial tension. We speculate that this is due to presence of the critical point of the reference (monomer) fluid, which is located inside the miscibility gap of the polymer solution, and inaccuracies in the description of the low density fluid. In the case of the surface free energy, there is an addition source of deviation: Since the SCF calculations describe the packing of the monomers at the surface only approximately, the SCF and MC calculations differ in the surface energies.

Having determined the excess free energies of surfaces and interfaces, we accurately locate the wetting transition temperature via the Young equation. We find a pronounced first order wetting transition, both in the Monte Carlo simulations and in the SCF calculation. We have located the concomitant prewetting line and obtained an estimate for the prewetting critical point. Evidence of 2D Ising critical behavior at the prewetting critical point is presented. Extrapolating the prewetting line back to the bulk coexistence is an alternative accurate strategy for locating the first order wetting transition. Since the SCF calculations agree only qualitatively with the MC results for the excess free energies, only qualitative agreement is achieved for the wetting transition temperature. In the Monte Carlo simulations the wetting occurs at a stronger attractive strength of the wall than in the SCF calculations and the prewetting line is less extended than in the SCF calculations.

Despite the quantitative deviations between the MC simulations and the SCF calculations the latter are very useful, because they require about 2 orders of magnitude less computational effort than the MC simulations. Therefore, they are an important tool for investigating the qualitative effects of system parameters. For instance, the SCF calculations show that it is unlikely to achieve a second-order wetting transition with a monomer−wall potential of the form $1/z^9 - f_w/z^3$ at $T = 1.68 \approx 0.84\ T_c$.

Having compared SCF calculations and MC simulations for a simple coarse-grained model, we intend to use this combination of techniques to explore more complex situations. A binary polymer solution in contact with a wall might exhibit an interesting interplay between wetting and phase separation and these systems have attracted recent experimental interest. Also ways of modifying the effective monomer wall interactions (e.g., by grafting a brush to the surface) and thereby changing the wetting properties of the surface are interesting topics.

Acknowledgment. It is a great pleasure to acknowledge stimulating discussions with K. Binder, who initiated this project. We have benefitted from discussions with O. Borisov, K. Mecke, L. Schäfer, M. Schick, F. Schmid, C. Vega, and K. Vollmayr-Lee. We acknowledge generous access to the CRAY T3E at the HLR Stuttgart and HLRZ Jülich, as well as access to the CONVEX SPP at the computing center in Mainz, Germany. Financial support was provided by the DFG under grant Bi314/17 in the framework of the program "Benetzung und

Strukturbildung an Grenzflächen". L.G.M. wishes to thank the University Complutense de Madrid for the award of a predoctoral grant and acknowledges financial support via the proyect PB97-0329 of the Spanish DGICYT.

References and Notes

(1) Binder, K. *Adv. Polym. Sci.* **1999**, *38*, 1.
(2) Jalbert, C.; Koberstein, J.; Hariharan, A.; Kumar, S. K. *Macromolecules* **1997**, *30*, 4481.
(3) Boltau, M.; Walheim, S.; Mlynek, J.; Krasch, G.; Steiner, U. *Nature* **1998**, *391*, 877.
(4) Huggins, M. L. *J. Chem. Phys.* **1941**, *9*, 440. Flory, P. G. *J. Chem. Phys.* **1941**, *9*, 660.
(5) Flory, P. J. *Principles of Polymer Chemistry*; Cornell University Press: Ithaca, NY, 1953.
(6) deGennes. P. G. *Scaling Concepts in Polymer Physics*; Cornell Univesity Press: Ithaca, NY, 1979.
(7) Duplantier, B. *J. Phys. (Fr.)* **1982**, *43*, 991; *J. Chem. Phys.* **1987**, *86*, 4233.
(8) Wilding, N. B.; Müller, M.; Binder, K. *J. Chem. Phys.* **1996**, *105*, 802.
(9) Frauenkron, H.; Grassberger, P. *J. Chem. Phys.* **1997**, *107*, 9599.
(10) Mackie, A. D.; Panagiotopoulos, A. Z.; Kumar, S. K. *J. Chem. Phys.* **1995**, *102*, 1014.
(11) Hager, J.; Schäfer, L. *Phys. Rev.* **1999**, *E60*, 2071.
(12) Enders, S.; Wolf, B. A.; Binder, K. *J. Chem. Phys.* **1995**, *103*, 3809.
(13) Dobashi, T.; Nakata, M.; Kaneko, M. *J. Chem. Phys.* **1980**, *72*, 6685 and 6692.
(14) Müller, M. *Macromol. Theory Simul.* **1999**, *8*, 343.
(15) Müller, M. *Macromolecules* **1998**, *31*, 9044.
(16) Sanchez, I. C.; Lacombe, R. H. *J. Phys. Chem.* **1976**, *80*, 2352.
(17) Schweizer, K. S.; Curro, J. G. *Adv. Chem. Phys.* **1997**, *98*, 1.
(18) Chatterjee, A. P.; Schweizer, K. S. *J. Chem. Phys.* **1998**, *108*, 3813.
(19) Chatterjee, A. P.; Schweizer, K. S. *Macromolecules* **1998**, *31*, 2353.
(20) Wertheim, M. S. *J. Chem. Phys.* **1987**, *87*, 7323.
(21) Johnson, J. K.; Zollweg, J. A.; Gubbins, K. E. *Mol. Phys.* **1993**, *3*, 591.
(22) Chapman, W. G.; Jackson, G.; Gubbins, K. S. *Mol. Phys.* **1988**, *65*, 1057.
(23) Stell, G.; Zhou, Y. *J. Chem. Phys.* **1989**, *91*, 3618.
(24) Stell, G.; Zhou, Y. *J. Chem. Phys.* **1992**, *96*, 1504 and 1507.
(25) MacDowell, L. G.; Vega, C. *J. Chem. Phys.* **1998**, *109*, 5670.
(26) Kierlik, E.; Rosinberg, M. L. *J. Chem. Phys.* **1992**, *97*, 9222; **1993**, *99*, 3950.
(27) Kierlik, E.; Rosinberg, M. L. *J. Chem. Phys.* **1993**, *100*, 1716.
(28) Sen, S.; Cohen, J. M.; McCoy, J. D.; Curro, J. G. *J. Chem. Phys.* **1994**, *101*, 9010; *102*, 3431.
(29) Nath, S. K.; McCoy, J. D.; Donley, J. P.; Curro, J. G. *J. Chem. Phys.* **1995**, *103*, 1635.
(30) Donley, J. P.; Rajasekaran, J. J.; McCoy, J. D.; Curro, J. G. *J. Chem. Phys.* **1995**, *103*, 5061.
(31) Woodward, C. E. *J. Chem. Phys.* **1991**, *94*, 3183.
(32) Woodward, C. E. *J. Chem. Phys.* **1992**, *97*, 695.
(33) Woodward, C. E.; Yethiraj, A. *J. Chem. Phys.* **1994**, *100*, 3181.
(34) Yethiraj, A.; Woodward, C. E. *J. Chem. Phys.* **1995**, *102*, 5499.
(35) Yethiraj, A. *J. Chem. Phys.* **1998**, *109*, 3269.
(36) McMullen, W. E.; Freed, K. F. *J. Chem. Phys.* **1990**, *92*, 1413.
(37) Yethiraj, A.; Hall, C. K. *J. Chem. Phys.* **1991**, *95*, 3749.
(38) Schmid, F. *J. Chem. Phys.* **1996**, *104*, 9191.
(39) Chandler, D.; McCoy, J. D.; Singer, S. J. *J. Chem. Phys.* **1986**, *85*, 5971.
(40) Nath, S. K.; McCoy, J. D.; Curro, J. G.; Saunders: R. S. *J. Chem. Phys.* **1997**, *106*, 1950. Nath, S. K.; Nealy, P. F.; dePablo, J. J. *J. Chem. Phys.* **1999**, *110*, 7483.
(41) Cahn, J. W.; Hilliard, J. E. *J. Chem. Phys.* **1958**, *28*, 258.
(42) MacDowell, L. G.; Müller, M.; Vega, C.; Binder, K. *J. Chem. Phys.* **2000**, in press.
(43) Kremer, K.; Grest, G. S. *J. Chem. Phys.* **1990**, *92*, 5057.
(44) Bennemann, C.; Paul, W.; Binder, K.; Dünweg, B. *Phys. Rev.* **1988**, *E 57* 843. Bennemann, C.; Paul, W.; Baschnagel, J.; Binder, K. *J. Phys. Condens. Matter* **1999**, *11*, 2179.
(45) Baschnagel, J.; et al. *Adv. Polym. Sci.* **2000**, *152*, 41. Tries, V.; Paul, W.; Baschnagel, K.; Binder, K. *J. Chem. Phys.* **1997**, *106*, 738.
(46) Pandey, R. B.; Milchev, A.; Binder, K. *Macromolecules* **1997**, *30*, 1194.
(47) Milchev, A.; Binder, K. *Eur. Phys. J.* **1998**, *B3*, 477.
(48) Alegandre, J.; Tildesley, D. J.; Chapela, G. A. *J. Chem. Phys.* **1995**, *102*, 4574; *Mol. Phys.* **1995**, *85*, 7726.
(49) Irving, J. H.; Kirkwood, J. G. *J. Chem. Phys.* **1950**, *18*, 817.
(50) Nijmeijer, M. J. P.; Bakker, A. F.; Bruin, C.; Sikkenk, J. H. *J. Chem. Phys.* **1988**, *89*, 3789.
(51) Siepmann, J. I. *Mol. Phys.* **1990**, *70*, 1145.
(52) Frenkel, D.; Mooij, G. C. A. M.; Smit, B. *J. Phys. Condens. Matter* **1992**, *3*, 3053.
(53) Laso, M.; dePablo, J. J.; Suter, U. W. *J. Chem. Phys.* **1992**, *97*, 2817.
(54) Borgs, C.; Kotecky, R. J. *Stat. Phys.* **1990**, *60*, 79; *Phys. Rev. Lett.* **1992**, *68*, 1734.
(55) Müller, M.; Wilding, N. B. *Phys. Rev.* **1994**, *E 57*, 2079. Müller, M.; Binder, K. *Comput. Phys. Commun.* **1994**, *84*, 173.
(56) Binder, K. *Phys. Rev.* **1992**, *A 25*, 1699.
(57) Berg, B. A.; Neuhaus, T. *Phys. Rev. Lett.* **1992**, *68*, 9. Berg, B. A.; Hansmann, U.; Neuhaus, T. *Z. Phys.* **1993**, *B90*, 229.
(58) Ferrenberg, A. M.; Swendson, R. H. *Phys. Rev. Lett.* **1988**, *61*, 2635; **1989**, *63*, 1195.
(59) Wang, J. S.; Tay, T. K.; Swendson R. H. *Phys. Rev. Lett.* **1999**, *82*, 486.
(60) Müller, M.; Binder, K. *Macromolecules* **1998**, *31*, 8323.
(61) Adams, P.; Henderson, J. R. *Mol. Phys.* **1991**, *73*, 1383. vanSwol, F.; Henderson, J. R. *Phys. Rev.* **1991**, *A 43*, 2932.
(62) DiMeglio, J. M.; Ober, R.; Paz, L.; Taupin, C.; Pincus, P.; Boileau, S. *J. Phys. (Fr.)* **1983**, *44*, 1035.
(63) Vrij, A. *J. Polym. Sci.* **1963**, *A2*, 1919.
(64) Lifshitz, I. M.; Grosberg, A. Y.; Kohklov, A. R. *Rev. Mod. Phys.* **1978**, *50*, 683.
(65) deGennes, P. G. *Macromolecules* **1981**, *14*, 1637. Eisenriegler, E. *J. Chem. Phys.* **1983**, *79*, 1052.
(66) Even if the density vanishes at a finite distance from the center of the interface, there is a fluctuation induced repulsion between the wall and the interface. Hence, the vapor wets the wall for $\epsilon_w = 0$.
(67) Young, T. *Philos. Trans. R. Soc. London* **1805**, *57*, 827.
(68) Curtin, W. A.; Ashcroft, N. W. *Phys. Rev.* **1985**, *A 32*, 2909; *Phys. Rev. Lett.* **1986**, *56*, 2775.
(69) Helfand, E.; Tagami, Y. *J. Chem. Phys.* **1972**, *56*, 3592. Helfand, E. *J. Chem. Phys.* **1975**, *62*, 999.
(70) Noolandi, J.; Hong, K. M. *Macromolecules* **1981**, *14*, 727; **1982**, *15*, 483.
(71) Shull, K. R. *Macromolecules* **1993**, *26*, 2346.
(72) Scheutjens, J. M. H. M.; Fleer, G. J. *J. Phys. Chem.* **1979**, *83*, 1619; **1979**, *84*, 178; *Macromolecules* **1985**, *18*, 1882.
(73) Matsen, M. W.; Schick, M. *Phys. Rev. Lett.* **1995**, *74*, 4225.
(74) Schmid, F. *J. Phys. Condens. Matter* **1998**, *10*, 8105.
(75) Szleifer, I.; Ben-Shaul, A.; Gelbhart, W. M. *J. Chem. Phys.* **1961**, *85*, 5345; **1987**, *86*, 7094.
(76) Szleifer, I. *Curr. Opin. Colloid Interface Sci.* **1997**, Z, 416. Szleifer, I.; Carignano, M. A. *Adv. Chem. Phys.* **1996**, *94*, 742.
(77) Müller, M.; Schick, M. *Macromolecules* **1996**, *29*, 8900.
(78) Müller, M.; Schick, M. *Phys. Rev. E* **1998**, *57*, 6973.
(79) Müller, M.; Werner, A. *J. Chem. Phys.* **1997**, *107*, 10764.
(80) Widom, B. *Science* **1967**, *375*, 157.
(81) Weeks, J. D.; Katsov, K.; Vollmayr, K. *Phys. Rev. Lett.* **1998**, *81*, 4400; Weeks, J. D.; Vollmayr, K.; Katsov, K. *Physica* **1997**, *A 244*, 461.
(82) Werner, A.; Schmid, F.; Müller, M.; Binder, K. *Phys. Rev.* **1999**, *E 59*, 728.
(83) Zhao, W.; Zhao, X.; Rafailivich, M. H.; Sokolov, J.; Composto, R. S.; Smith, S. D.; Satkowski, M.; Russel, T. P.; Dozier, W. D.; Mansfeld, T. *Macromolecules* i**1993**, *26*, 561.
(84) Plischke, M.; Henderson, D. *J. Chem. Phys.* **1986**, *84*, 2846.
(85) Bitsanis, I.; Hadziioannou, G. *J. Chem. Phys.* **1990**, *92*, 3827.
(86) Baschnagel, J.; Binder, K. *Macromolecules* **1995**, *28*, 6808.
(87) Buff, F. P.; Lovett, P. A.; Stillinger, F. H. *Phys. Rev. Lett.* **1965**, *15*, 621. Weeks, J. D. *J. Chem. Phys.* **1977**, *67*, 3106. Bedeaux, D.; Weeks, J. D. *Ibid.* **1985**, *82*, 972.
(88) Müller, M.; Schick, M. *J. Chem. Phys.* **1996**, *105*, 8885 and 8282.
(89) Mecke, K.; Dietrich, S. *Phys. Rev.* **1999**, *E 59*, 6766.
(90) Wang, S.; Tolan, M.; Seeck, O. H.; Sinha, S. K.; Bahr, O.; Rafailovich, M. H.; Sokolov, J. *Phys. Rev. Lett.* **1999**, *83*, 564. Tolan, M.; Seeck, O. H.; Schlomka, J.-P.; Press, W.; Wang, S.; Sinha, S. K.; Li, Z.; Rafailovich, M. H.; Sokolov, J. *Phys. Rev. Lett.* **1998**, *81*, 2731. See also: Tolan, M. *X-ray Scattering from Soft-Matter Thin Films*; Springer Tracts in Modern Physics; Springer: Berlin, 1999; Vol. 148.
(91) Sanyal, M. K.; Sinha, S. K.; Huang, K. G.; Ocko, B. M. *Phys. Rev. Lett.* **1991**, *66*, 628.

(92) Tidswll, I. M.; Rabedeau, T. A.; Reshan, P. S.; Kosowski, S. D. *Phys. Rev. Lett.* **1991**, *66*, 2108.

(93) One could try to locate the local interfacial position by dividing the systems into columns of size $B \times B \times D$ and then to average the profile in each column with respect to the local interface position in this column.[82] Choosing B small enough, one minimizes the effect of capillary waves. This enables one to compare directly the profile in a column with the intrinsic profile of the SCF calculation. However, the value $s = 1.9$ required to map the SCF calculation onto the laterally averaged MC profile suggests a choice of B as small as 2.1σ. If we assume bulklike density fluctuations, then these "intrinsic" fluctuations in a subvolume of the size 2.1 $\times$ 2.1 $\times$ 9 amount to $\sqrt{\langle(\phi-\langle\phi\rangle)^2\rangle} \approx 0.2\langle\phi\rangle$. Using an integral criterion to locate the local interface position in such a small subvolume results in a fluctuation in the position of the order 1.8σ due to bulklike fluctuations. This is comparable to the contribution of capillary waves on the whole lateral extension. Any local criterion (like a crossing criterion) applied to the profile in the subcolum also fails, because the 24 monomers which are located on average in each subcolumn do not yield a smooth instantaneous profile.

(94) Werner, A.; Schmid, F.; Müller, M.; Binder, K. *J. Chem. Phys.* **1997**, *107*, 8175.

(95) Schick, M. *Les Houches lectures on "Liquids at Interfaces"*; Elsevier Science Publishers B. V.: Amsterdam, 1990. Dietrich, S. In *Phase Transitions and Critical Phenomena*; Domb, C., Lebowitz, J. L., Eds.; Academic Press: New York, 1988; Vol 14.

(96) Cahn, J. W. *J. Chem. Phys.* **1977**, *66*, 3667.

(97) Bruin, S.; Nijmeijer, M. J. P.; Crevecoeur, R. M. *J. Chem. Phys.* **1995**, *102*, 7622.

(98) Hauge, E. H.; Schick, M. *Phys. Rev.* **1983**, *B 27*, 4288.

(99) Binder, K. *Phys. Rev. Lett.* **1981**, *47*, 693.

(100) Wilding, N. B. *Phys. Rev.* **1995**, *E52*, 602.

MA991796T